CrossMark

J. Fluid Mech. (2017), *vol.* 819, *pp.* 58–103. © Cambridge University Press 2017
doi:10.1017/jfm.2017.164

Direct numerical simulation of scalar transport in turbulent flows over progressive surface waves

Di Yang[1] **and Lian Shen**[2,†]

[1]Department of Mechanical Engineering, University of Houston, Houston, TX 77204, USA

[2]Department of Mechanical Engineering and St. Anthony Falls Laboratory, University of Minnesota, Minneapolis, MN 55455, USA

(Received 2 July 2016; revised 7 March 2017; accepted 11 March 2017;
first published online 18 April 2017)

The transport of passive scalars in turbulent flows over progressive water waves is studied using direct numerical simulation. A combined pseudo-spectral and finite-difference scheme on a wave-surface-fitted grid is used to simulate the flow and scalar fields above the wave surface. Three representative wave ages (i.e. wave-to-wind speed ratios) are considered, corresponding to slow, intermediate and fast wind-waves, respectively. For each wave condition, four Schmidt numbers are considered for the scalar transport. The presence of progressive surface waves is found to induce significant wave-phase-correlated variation to the scalar field, with the phase dependence varying with the wave age. The time- and plane-averaged profiles of the scalar over waves of various ages exhibit similar vertical structures as those found in turbulence over a flat wall, but with the von Kármán constant and effective wave surface roughness for the mean scalar profile exhibiting considerable variation with the wave age. The profiles of the root-mean-square scalar fluctuations and the horizontal scalar flux exhibit good scaling in the viscous sublayer that agrees with the scaling laws previously reported for flat-wall turbulence, but with noticeable wave-induced variation in the viscous wall region. The profiles of the vertical scalar flux in the viscous sublayer exhibit apparent discrepancies from the reported scaling law for flat-wall turbulence, due to a negative vertical flux region above the windward face of the wave crest. Direct observation and quadrant-based conditional averages indicate that the wave-dependent distributions of the scalar fluctuations and fluxes are highly correlated with the coherent vortical structures in the turbulence, which exhibit clear wave-dependent characteristics in terms of both shape and preferential location.

Key words: turbulent boundary layers, turbulence simulation, wind–wave interactions

1. Introduction

The air–sea exchange of scalar quantities, such as water vapour and heat, near the air–water interface plays a vital role in global and regional air–sea interactions (Smith 1988; DeCosmo *et al.* 1996; Fairall *et al.* 1996; Edson *et al.* 2007). Turbulent transport of scalars in the air above the sea surface is strongly affected by the

† Email address for correspondence: shen@umn.edu

https://doi.org/10.1017/jfm.2017.164 Published online by Cambridge University Press

surface waves. The periodical surface curvatures and the motions of these waves can induce considerable disturbance to the air turbulent flows near the wave surface, affecting the transport of both momentum and scalars (Edson *et al.* 2007; Sullivan & McWilliams 2010).

Various experimental studies have been conducted in the past several decades to characterize the effect of sea-surface waves on air–sea scalar transport. For example, Fairall *et al.* (1996), Bourassa, Vincent & Wood (1999) and Edson *et al.* (2004) measured the bulk properties of the air–sea scalar exchange, and parameterized the scalar flux profiles in terms of averaged air–sea interfacial properties such as the scalar transfer coefficient, sea-surface scalar roughness length, and convective scaling velocity. Edson *et al.* (2007) measured the velocity, temperature and relative humidity in the marine atmospheric boundary layer (ABL) under low winds in the CBLAST-LOW experiment. Based on the CBLAST-LOW data, Katsouvas, Helmis & Wang (2007) performed quadrant analysis for the scalar and momentum fluxes. Katul, Sempreviva & Cava (2008) analyzed the data from RASEX (Risø Air Sea EXperiment) and developed a one-dimensional model for the temperature–humidity covariance. Experimental studies of air–sea scalar transport have provided valuable insights and parameterizations for modelling air–sea interactions.

In recent years, enabled by the continuous advancement of computer power, numerical simulation has become a valuable tool for studying the fine-scale scalar transport phenomena near the air–water interface. Modelling the air turbulence over sea surfaces is challenging, primarily due to the difficulty associated with modelling the effect of sea-surface waves. One approach is to approximate the marine ABL as turbulence over a flat surface, with the wave effect parameterized as the sea-surface roughness length (e.g. Charnock 1955; Fairall *et al.* 1996). However, accurately parameterizing the sea-surface roughness is found to be quite challenging due to the complexity in wind–wave interaction (e.g. Donelan 1990; Toba, Smith & Ebuchi 2001; Yang, Meneveau & Shen 2013). Instead, many previous numerical studies attempted to directly simulate air turbulence over progressive surface waves, with the instantaneous wave motions imposed in the simulation as bottom boundary conditions (e.g. Sullivan, McWilliams & Moeng 2000; Sullivan & McWilliams 2002; Kihara *et al.* 2007; Yang & Shen 2009, 2010; Druzhinin, Troitskayaa & Zilitinkevich 2016). Most of these previous studies focused on the momentum transfer between the air turbulence and the water waves. Sullivan & McWilliams (2002) and Druzhinin *et al.* (2016) considered the temperature field in their simulations with a Prandtl number of 0.7, corresponding to the ratio of kinematic viscosity to thermal diffusivity of the air, and studied the effects of various stratification conditions (characterized by the Richardson number) on the characteristics of the air turbulence. On the other hand, a number of numerical studies have been performed focusing on the statistics of scalar fluctuations over stationary wavy walls (e.g. Antonia & Kim 1991; Kawamura *et al.* 1998; Dellil, Azzi & Jubran 2004; Park, Choi & Suzuki 2004; Choi & Suzuki 2005; Rossi 2010). These studies have shown significant effects of the stationary waves on the characteristics of scalar transport, such as the surface scalar flux, the mean scalar concentration, the scalar variance and the turbulent scalar fluxes. However, there is still a lack of studies devoted to the mechanism of scalar transport in turbulence over progressive surface waves, which is expected to be significantly different from the cases with stationary wavy walls (Belcher & Hunt 1998; Sullivan & McWilliams 2010).

In this study, the direct numerical simulation (DNS) solver developed by Yang & Shen (2011*a*) is adopted, which uses a boundary-fitted computational grid system

https://doi.org/10.1017/jfm.2017.164 Published online by Cambridge University Press

that follows the instantaneous wave surface elevation and motions, allowing one to resolve the details of the turbulent flow above and in the vicinity of the mobile wave surface. In the present study, this DNS solver is further expanded by including a scalar transport solver within the boundary-fitted spatial discretization framework, and is used to simulate the transport of passive scalars in turbulent flows over progressive surface waves. As in many recent numerical studies, a plane progressive surface wave train is imposed at the bottom of the simulation domain (e.g. Sullivan *et al.* 2000, 2008; Sullivan & McWilliams 2002; Kihara *et al.* 2007; Yang & Shen 2009, 2010; Hara & Sullivan 2015; Druzhinin *et al.* 2016). A relatively large wave steepness of $ak = 0.25$ is considered, where a is the wave amplitude and k is the wavenumber. To account for the nonlinearity associated with such a steep wave, a high-order Stokes wave solution is used to prescribe the wave surface elevation and orbital velocity. Three representative wave-to-wind speed ratios c/u_* (also called the wave age) are considered, including $c/u_* = 2$ (slow waves), 14 (intermediate waves) and 25 (fast waves), where c is the wave phase speed and u_* is the friction velocity of the turbulence. In order to achieve the desired value for c/u_*, the turbulent flow is driven by a constant streamwise stress applied at the top flat boundary, and the mean flow has a Couette-flow-type of velocity profile, but with the mean velocity at the top boundary varying for different wave conditions. The scalar transport is known to be largely affected by the Schmidt number $Sc = \nu/D$, where ν is the kinematic viscosity and D is the scalar molecular diffusivity. For each wave condition, four Schmidt numbers are considered, including $Sc = 0.5$, 1.0, 2.0 and 4.0. Based on the DNS data, the effects of surface waves on the scalar transport are studied by various statistical analysis techniques, including time and plane average, wave phase average, quadrant analysis and conditional average. The correlations between coherent vortical structures and turbulent scalar transport events are also studied by direct observation of instantaneous snapshots and quadrant-based conditional averages.

The remainder of this paper is organized as follows. First, the mathematical formulas and numerical schemes of the DNS solver are described in § 2. Then the configurations of the simulation cases are given in § 3, together with some sample results of the DNS. In § 4, various types of statistical analyses of the DNS data are performed, and the effects of surface waves on the characteristics of flow structures and turbulent scalar transport are discussed. Finally, conclusions are given in § 5.

2. Description of DNS

As shown in figure 1, this study uses DNS to examine the transport of passive scalars in a three-dimensional stress-driven turbulent Couette flow over a plane progressive surface wave train. The Cartesian coordinates are denoted as $x_i(i = 1, 2, 3) = (x, y, z)$, where x and y are the horizontal coordinates and z is the vertical coordinate, with $z = 0$ being the mean elevation of the surface wave at the bottom of the simulation domain; $u_i(i = 1, 2, 3) = (u, v, w)$ are the corresponding velocity components in x-, y- and z-directions, respectively.

In the simulation, the flow is driven by a constant streamwise shear stress τ_x prescribed on the rigid flat top boundary, which prescribes a fixed turbulence friction velocity of $u_* = \sqrt{\tau_x/\rho}$, where ρ is the fluid density. The bottom of the flow is bounded and distorted by a two-dimensional wave train that propagates in the x-direction. This stress-driven Couette flow configuration has been used as a canonical problem to study the surface water wave effect on turbulent air flows in many previous numerical studies (e.g. Gent & Taylor 1976; Li, Xu & Taylor 2000;

https://doi.org/10.1017/jfm.2017.164 Published online by Cambridge University Press

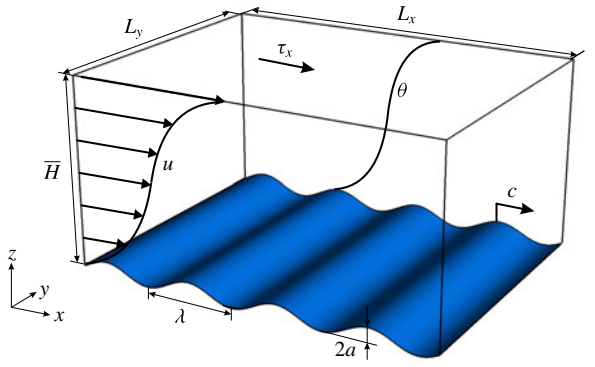


FIGURE 1. (Colour online) Sketch of the simulation configuration. A three-dimensional turbulent Couette flow is driven by a constant shear stress τ_x applied at the top boundary, and flows over a plane progressive surface wave train. The surface wave has a wavelength λ and an amplitude a. The wave propagates in the x-direction with a phase speed c. The passive scalar field θ is transported by the turbulent Couette flow, with Dirichlet boundary conditions of $\theta = 0$ and $\theta = 2$ at the bottom and top boundaries, respectively.

Kihara *et al.* 2007; Yang & Shen 2009, 2010). A passive scalar θ is transported by the turbulent flow, with a Dirichlet boundary condition of $\theta = 0$ on the bottom wave surface and $\theta = 2$ on the top boundary. This configuration for θ results in $\theta \approx 1$ at the centre of the simulation domain. We remark that in this canonical simulation configuration, we set the passive scalar to have a smaller value near the wave surface and a larger value near the upper boundary, similar to many previous numerical studies (e.g. Dellil *et al.* 2004; Park *et al.* 2004; Rossi 2010). In some applications, e.g. the moisture in the marine atmospheric boundary layer, the scalars have higher concentrations near the wave surface. Because θ is assumed to be passive and its governing equation is linear with respect to θ, the results reported in this study can be converted to the reversed configuration with a larger scalar value near the wave surface. We choose the current configuration as it allows us to compare the current DNS results to the previously reported results of passive scalar transport in turbulent boundary layers over flat and wavy boundaries.

In the DNS, the turbulent carrier flow is described by the three-dimensional incompressible Navier–Stokes equations

$$\frac{\partial u_i}{\partial x_i} = 0, \tag{2.1}$$

$$\frac{\partial u_i}{\partial t} + \frac{\partial (u_i u_j)}{\partial x_j} = -\frac{1}{\rho}\frac{\partial p}{\partial x_i} + \nu \frac{\partial^2 u_i}{\partial x_j \partial x_j}, \tag{2.2}$$

where p is the pressure. The transport of the passive scalar $\theta(x, y, z, t)$ is governed by a convection–diffusion equation

$$\frac{\partial \theta}{\partial t} + \frac{\partial (\theta u_j)}{\partial x_j} = D \frac{\partial^2 \theta}{\partial x_j \partial x_j}. \tag{2.3}$$

The effect of progressive surface waves on the turbulence is imposed through a Dirichlet velocity boundary condition at the bottom wave surface, $u_i(z = \eta) = (u_s, v_s, w_s)$, where η is the wave surface elevation and (u_s, v_s, w_s) are the wave

https://doi.org/10.1017/jfm.2017.164 Published online by Cambridge University Press

surface orbital velocities. In this study, we use a high-order two-dimensional Stokes wave solution to prescribe the motions of the plane-progressive surface wave train (Stokes 1847),

$$\eta(x, y, t) = \sum_{n=1}^{N} (ak)^{n-1} \eta^{(n)}(x, y, t), \tag{2.4}$$

$$u_s(x, y, t) = \sum_{n=1}^{N} (ak)^{n-1} u_s^{(n)}(x, y, t), \tag{2.5}$$

$$v_s(x, y, t) = 0, \tag{2.6}$$

$$w_s(x, y, t) = \sum_{n=1}^{N} (ak)^{n-1} w_s^{(n)}(x, y, t), \tag{2.7}$$

where the variables with superscript '(n)' indicate the nth mode of the corresponding wave quantity. In particular, following Dommermuth & Yue (1987), we directly solve the nonlinear equations associated with the mapping function in Schwartz (1974) by using Newton iteration up to a high order of $N = 192$. As a reference, the Stokes solution up to the second order can be found in Dean & Dalrymple (1991). For the purpose of defining some key parameters of the wave boundary conditions, in the following equations only the leading order mode of the Stokes wave solution is given, which is the same as the Airy wave solution and has been used in many prior DNS studies (e.g. Sullivan *et al.* 2000, 2008; Kihara *et al.* 2007; Hara & Sullivan 2015; Druzhinin *et al.* 2016):

$$\eta^{(1)}(x, y, t) = a \sin\, k(x - ct), \tag{2.8}$$

$$u_s^{(1)}(x, y, t) = akc\, \sin k(x - ct), \tag{2.9}$$

$$v_s^{(1)}(x, y, t) = 0, \tag{2.10}$$

$$w_s^{(1)}(x, y, t) = akc\, \cos k(x - ct). \tag{2.11}$$

Here, a is the amplitude of the leading wave mode, $k = 2\pi/\lambda$ is its wavenumber, λ is its wavelength, and c is its phase speed.

We note that the current DNS solver can be dynamically coupled with another solver for the water waves, allowing the simulation of turbulence with a dynamically evolving wave field (Yang & Shen 2011*b*). Because this study focuses on understanding the fundamental mechanisms of the surface wave effects on the passive scalar transport, we choose to use the canonical configuration with a prescribed Stokes wave boundary condition, which allows for a precise phase average based on the periodic wave form and yields well-converged statistics for the flow and scalar fields. Moreover, when a more realistic dynamically evolving wave field (either monochromatic or broadband) is considered, a realistically high Reynolds number should be considered in order to capture the interaction between turbulence and surface waves over a wide range of scales, for which the flow and scalar fields have to be simulated using wall-modelled large-eddy simulation (Yang *et al.* 2013; Yang, Meneveau & Shen 2014*a*,*b*). These more realistic and complicated conditions go beyond the scope of the current canonical study, but are worth considering in future studies of scalar transport in turbulent wind over ocean waves.

To capture the surface wave effect on the scalar field, the DNS solver uses a boundary-fitted coordinate system that follows the instantaneous deformation of the

https://doi.org/10.1017/jfm.2017.164 Published online by Cambridge University Press

wave surface. The irregular wave surface-bounded domain in the physical space (x, y, z, t) is transformed to a right rectangular prism in the computational space (ξ, ψ, ζ, τ) with the following algebraic mapping:

$$\xi = x, \quad \psi = y, \quad \zeta = \frac{z - \eta(x, y, t)}{H(x, y, t)} = \frac{z - \eta(x, y, t)}{\overline{H} - \eta(x, y, t)}, \quad \tau = t. \tag{2.12a–d}$$

Here, the height of the physical domain, $H(x, y, t)$, is decomposed into an average height $\overline{H}$ and a wave induced variation $-\eta(x, y, t)$. Similar to x_i, the spatial coordinates in the computational space can also be denoted using the index notation as $\xi_i (i = 1, 2, 3) = (\xi, \psi, \zeta)$.

The Jacobian matrix of the spatial coordinate transformation is

$$\boldsymbol{J} = \begin{bmatrix} \dfrac{\partial \xi}{\partial x} & \dfrac{\partial \xi}{\partial y} & \dfrac{\partial \xi}{\partial z} \\ \dfrac{\partial \psi}{\partial x} & \dfrac{\partial \psi}{\partial y} & \dfrac{\partial \psi}{\partial z} \\ \dfrac{\partial \zeta}{\partial x} & \dfrac{\partial \zeta}{\partial y} & \dfrac{\partial \zeta}{\partial z} \end{bmatrix} = \begin{bmatrix} 1 & 0 & 0 \\ 0 & 1 & 0 \\ \dfrac{\zeta - 1}{\overline{H} - \eta} \dfrac{\partial \eta}{\partial x} & \dfrac{\zeta - 1}{\overline{H} - \eta} \dfrac{\partial \eta}{\partial y} & \dfrac{1}{\overline{H} - \eta} \end{bmatrix}. \tag{2.13}$$

Because the wave surface oscillates in time, a transformation is also required for the temporal derivative terms, i.e.

$$\frac{\partial}{\partial t} = \frac{\partial}{\partial \tau} + \frac{\partial \zeta}{\partial t} \frac{\partial}{\partial \zeta}, \quad \text{where } \frac{\partial \zeta}{\partial t} = \frac{\zeta - 1}{\overline{H} - \eta} \frac{\partial \eta}{\partial t}. \tag{2.14}$$

By applying the chain rule together with (2.13) and (2.14), we write the governing equations (2.1)–(2.3) in the wave-surface-fitted coordinates as

$$J_{kj} \frac{\partial u_j}{\partial \xi_k} = 0, \tag{2.15}$$

$$\frac{\partial u_i}{\partial \tau} + \delta_{j3} \frac{\partial \zeta}{\partial t} \frac{\partial u_i}{\partial \xi_j} + J_{kj} \frac{\partial (u_i u_j)}{\partial \xi_k} = -\frac{J_{ki}}{\rho} \frac{\partial p}{\partial \xi_k} + \nu J_{nj} \frac{\partial}{\partial \xi_n} \left(J_{kj} \frac{\partial u_i}{\partial \xi_k} \right), \tag{2.16}$$

$$\frac{\partial \theta}{\partial \tau} + \delta_{j3} \frac{\partial \zeta}{\partial t} \frac{\partial \theta}{\partial \xi_j} + J_{kj} \frac{\partial (\theta u_j)}{\partial \xi_k} = D J_{nj} \frac{\partial}{\partial \xi_n} \left(J_{kj} \frac{\partial \theta}{\partial \xi_k} \right), \tag{2.17}$$

where J_{ij} is the index notation of the matrix $\boldsymbol{J}$ and δ_{ij} is the Kronecker delta. Note that u_i are the velocities in the physical space.

In DNS, equations (2.15)–(2.17) are discretized in the computational space (ξ, ψ, ζ, τ) and solved numerically. In particular, a Fourier-series-based pseudo-spectral method is used in the (ξ, ψ)-plane, with evenly spaced collocated grid points in both directions. The standard 2/3-rule is used for eliminating the aliasing error. In the vertical direction, a second-order finite-difference method is used based on a staggered ζ-grid. The vertical grid is clustered near the top boundary and the bottom wave surface to provide adequate resolution for the boundary layers. The governing equations are integrated in time with a fractional-step method. For both (2.16) and (2.17), the nonlinear convection terms are advanced in time using a second-order Adams–Bashforth scheme. In order to resolve the boundary layer without requiring a significantly small timestep, a semi-implicit scheme is desired for

https://doi.org/10.1017/jfm.2017.164 Published online by Cambridge University Press

time advancement of the viscous diffusion terms in (2.16) and (2.17). Due to the coordinate transformation (2.12), in the computational space the Laplacian operator in the diffusion terms becomes

$$\nabla^2 = J_{nj}\frac{\partial}{\partial\xi_n}\left(J_{kj}\frac{\partial}{\partial\xi_k}\right) = \underbrace{\frac{\partial^2}{\partial\xi^2}+\frac{\partial^2}{\partial\psi^2}+2J_{31}\frac{\partial^2}{\partial\xi\partial\zeta}+2J_{32}\frac{\partial^2}{\partial\psi\partial\zeta}}_{\nabla^2_{\xi\psi}} + \underbrace{\left(J_{31}^2+J_{32}^2+J_{33}^2\right)\frac{\partial^2}{\partial\zeta^2}+\left(\frac{\partial^2\zeta}{\partial x^2}+\frac{\partial^2\zeta}{\partial y^2}\right)\frac{\partial}{\partial\zeta}}_{\nabla^2_{\zeta}}, \tag{2.18}$$

where

$$\frac{\partial^2\zeta}{\partial x^2} = \frac{\zeta-1}{\overline{H}-\eta}\frac{\partial^2\eta}{\partial x^2}+\frac{2(\zeta-1)}{(\overline{H}-\eta)^2}\left(\frac{\partial\eta}{\partial x}\right)^2, \tag{2.19}$$

$$\frac{\partial^2\zeta}{\partial y^2} = \frac{\zeta-1}{\overline{H}-\eta}\frac{\partial^2\eta}{\partial y^2}+\frac{2(\zeta-1)}{(\overline{H}-\eta)^2}\left(\frac{\partial\eta}{\partial y}\right)^2. \tag{2.20}$$

In the Laplacian operator (2.18), the first part, $\nabla^2_{\xi\psi}$, involves derivatives with respect to ξ and ψ, and is thus treated with the second-order Adams–Bashforth scheme; the second part, ∇^2_{ζ}, is treated semi-implicitly using the Crank–Nicolson scheme. Note that if the Crank–Nicolson scheme is used for the entire diffusion term and if the momentum equations are solved by the pseudo-spectral method, the presence of the several Jacobian coefficients J_{ij} in (2.18) would require (2.16) and (2.17) to be solved iteratively. The use of the above hybrid scheme helps to avoid iteration, and meanwhile keeps the dominant diffusion terms $\nu\nabla^2_{\zeta}u_i$ and $D\nabla^2_{\zeta}\theta$ semi-implicit. Compared with a pure explicit scheme, this hybrid scheme relaxes the numerical stability constraint on the simulation timestep when using a refined vertical grid to adequately resolve the boundary layer. For the velocity field, the incompressibility constraint (2.15) is satisfied by constructing and solving a Poisson equation for the pressure and then adding pressure correction terms to the velocity components. Note that because of the non-constant coefficients in the Laplacian operator (2.18), the pressure Poisson equation needs to be solved iteratively.

We also remark that while (2.2) and (2.3) are written in the conservative form, after the coordinate transformation, (2.16) and (2.17) are in a weakly conservative form. A strongly conservative form can be further derived by first dividing (2.16) and (2.17) by the Jacobian and then rearranging all the terms into the forms of derivatives of the primary variables with respect to the independent variables (ξ, ψ, ζ, τ) (e.g. Vinokur 1974; Anderson, Tannehill & Pletcher 1984; Zang, Street & Koseff 1994; Sullivan *et al.* 2000). Nevertheless, the above numerical scheme is found to provide accurate results, especially for air flows over water waves, with relatively low computational cost. Extensive validation and detailed discussion on the performance of the numerical scheme can be found in Yang & Shen (2011*a*,*b*). Additional validations for turbulent flows and scalar transport over a flat wall are given in appendix A.

3. Simulation configuration

For the simulations of turbulent flows over surface waves considered in this study, the flow is driven by a constant shear stress τ_x applied on the top boundary of the

https://doi.org/10.1017/jfm.2017.164 Published online by Cambridge University Press

simulation domain. The Reynolds number based on the friction velocity $u_* = \sqrt{\tau_x/\rho}$ and half of the mean domain height $\delta = \overline{H}/2$ is $Re_* = u_*\delta/\nu = 445$. To capture the effect of surface waves on the turbulence transport of scalars, a computational domain of $\left(L_x, L_y, \overline{H}\right) = (4\lambda, 3\lambda, 2\lambda)$ is used, where the wavelength $\lambda = \delta$. This domain size has been found to be sufficiently large based on the test of two-point spatial correlation (Yang & Shen 2009). The domain is transformed into the computational space (ξ, ψ, ζ) based on (2.12), and then discretized using 192^3 grid points. In particular, the grid points are evenly spaced in the ξ- and ψ-directions, providing grid resolutions of $\Delta\xi^+ = 9.27$ and $\Delta\psi^+ = 6.95$, respectively (here the subscript '+' denotes the length in wall unit, i.e. normalized by ν/u_*). In the vertical direction, the grid points are clustered near the bottom and top boundaries with $\Delta\zeta^+ = 0.4$, and become coarsely spaced towards the centre of the domain with $\Delta\zeta^+ = 8.7$.

Note that the Reynolds number considered in the current DNS study is lower than those used in DNS studies of turbulence over a flat surface (e.g. Hoyas & Jiménez 2006; Lee & Moser 2015) because of the additional complexity and computational cost caused by the boundary-fitted grid and coordinate transformation, but is higher than those used in many previous DNS studies of turbulence over progressive and stationary waves, e.g. $Re_* = 171$ in De Angelis, Lombardi & Banerjee (1997), $Re_* = 100 \sim 164$ in Sullivan *et al.* (2000) and Sullivan & McWilliams (2002), $Re_* = 150$ in Kihara *et al.* (2007), $Re_* = 283$ in Yang & Shen (2010), and $Re_* = 140 \sim 325$ in Druzhinin, Troitskaya & Zilitinkevich (2012) and Druzhinin *et al.* (2016). Although limited to relatively low Reynolds numbers, DNS has been found to be able to reproduce many key features of laboratory experiments and field observations (Sullivan & McWilliams 2010). More importantly, DNS directly resolves the flow and scalar transport in the near-surface region, where molecular viscosity and diffusivity play an important role. Meirink & Makin (2000) solved the Reynolds-averaged Navier–Stokes equations using a Dirichlet wave boundary condition and a second-order closure of Craft & Launder (1996) that is valid in the viscous sublayer, and reproduced the air flow over water waves measured by Stewart (1970), suggesting the importance of capturing the viscous effect when modelling wind–wave interaction (Sullivan & McWilliams 2010).

Because DNS usually uses relatively low Reynolds numbers to resolve all the essential turbulence motions at different scales, the velocity and length scales considered in the present and other similar studies in literature do not directly match the real scales in wind over water waves. Nevertheless, DNS has been proven to provide valuable insights for understanding the characteristics of wind turbulence over waves. Moreover, previous studies have shown that the wave age, defined as the ratio of the wave phase speed c to a characteristic wind velocity, is a key parameter for the quantitative description of wind–wave interaction (see the reviews by Belcher & Hunt 1998; Sullivan & McWilliams 2010). Typical choices of the characteristic wind velocity include: (1) the wind friction velocity, u_* (e.g. Belcher & Hunt 1998; Sullivan *et al.* 2000; Kihara *et al.* 2007; Yang & Shen 2009, 2010); (2) the mean wind velocity at a height proportional to the wavelength λ, e.g. U_λ at $z = \lambda$ or $U_{\lambda/2}$ at $z = \lambda/2$ (e.g. Sullivan *et al.* 2000; Donelan *et al.* 2006); and (3) the mean wind velocity at a fixed height above the mean wave surface regardless of the wavelength, e.g. U_{10} at the 10 m height (see, e.g., Hristov, Miller & Friehe 2003; Donelan *et al.* 2006, among others). In this study, because the carrier flow is driven by a prescribed stress τ_x that gives a constant friction velocity u_*, it is most convenient to define the wave age as c/u_*.

To study the effect of surface wave motion on the scalar transport, three different wave ages are considered, $c/u_* = 2$, 14 and 25, corresponding to the young,

https://doi.org/10.1017/jfm.2017.164 Published online by Cambridge University Press

Case	Type	c/u_*	κ	z_0^+	B	Sc	κ_θ	$z_{0,\theta}^+$	B_θ
S25	stationary	0	0.43	1.21	−0.44	0.5	0.48	1.22	−0.41
	sinusoidal					1.0	0.48	2.09×10^{-1}	3.27
	wave					2.0	0.48	1.54×10^{-2}	8.72
						4.0	0.48	3.09×10^{-4}	17.01
W25C2	Stokes wave	2	0.39	2.31	−2.17	0.5	0.43	1.89	−1.46
						1.0	0.42	4.69×10^{-1}	1.79
						2.0	0.41	6.35×10^{-2}	6.64
						4.0	0.41	3.27×10^{-3}	14.08
W25C14	Stokes wave	14	0.39	0.22	3.84	0.5	0.46	7.06×10^{-1}	0.75
						1.0	0.46	8.49×10^{-2}	5.42
						2.0	0.45	3.46×10^{-3}	12.63
						4.0	0.44	2.82×10^{-5}	23.97
W25C25	Stokes wave	25	0.27	0.55	2.24	0.5	0.35	1.76	−1.60
						1.0	0.33	3.91×10^{-1}	2.81
						2.0	0.31	4.52×10^{-2}	9.85
						4.0	0.29	2.14×10^{-3}	21.40

TABLE 1. List of DNS cases for turbulent flow over stationary and Stokes waves with steepness $ak = 0.25$ and Reynolds number $Re_* = 445$. In the table, the parameters without and with subscript 'θ' are for mean velocity and scalar profiles, respectively. In particular, κ is the von Kármán constant, z_0^+ is the effective wave surface roughness, and B is the profile offset. Detailed discussions of the mean profiles are given in § 4.3.

intermediate and mature stages of wind-generated waves, respectively (Belcher & Hunt 1998). Moreover, if $c = 0$, the bottom boundary becomes a stationary wavy wall without orbital motion, which has often been used as a reference case for comparison in many prior numerical studies of flows over surface waves. All of the four wave cases have a wave steepness of $ak = 0.25$. The wave cases considered in the present study are summarized in table 1. For each wave case, four Schmidt numbers, $Sc = 0.5$, 1.0, 2.0 and 4.0, are considered in the DNS for the scalar transport. Figure 2 shows some sample DNS results for the instantaneous scalar concentration field in turbulence over the four different types of waves with $Sc = 1.0$. Apparent differences in the instantaneous scalar field can be observed among the stationary (S25), slow (W25C2) and intermediate (W25C14) wave cases, while the difference between the intermediate and fast (W25C25) wave cases is less obvious. To quantitatively study the effect of surface waves on scalar transport, in the next section various statistical analyses are performed for the scalar field. For data sampling, in all the cases the simulations were carried out for approximately 34 000 viscous time units (i.e. tu_*^2/ν). Three-dimensional snapshots of instantaneous velocity and scalar fields were outputted for every 20 viscous time units starting from approximately 26 000 viscous time units, with totally 400 instantaneous snapshots sampled for the statistical analyses.

4. Results

4.1. *Phase-averaged scalar field*

To quantify the effect of surface waves on the turbulent flow and scalar fields, a triple decomposition is applied to analyze the instantaneous quantities. Specifically, an instantaneous quantity $f(x, y, z, t)$ obtained from the DNS can be decomposed as (e.g.

https://doi.org/10.1017/jfm.2017.164 Published online by Cambridge University Press

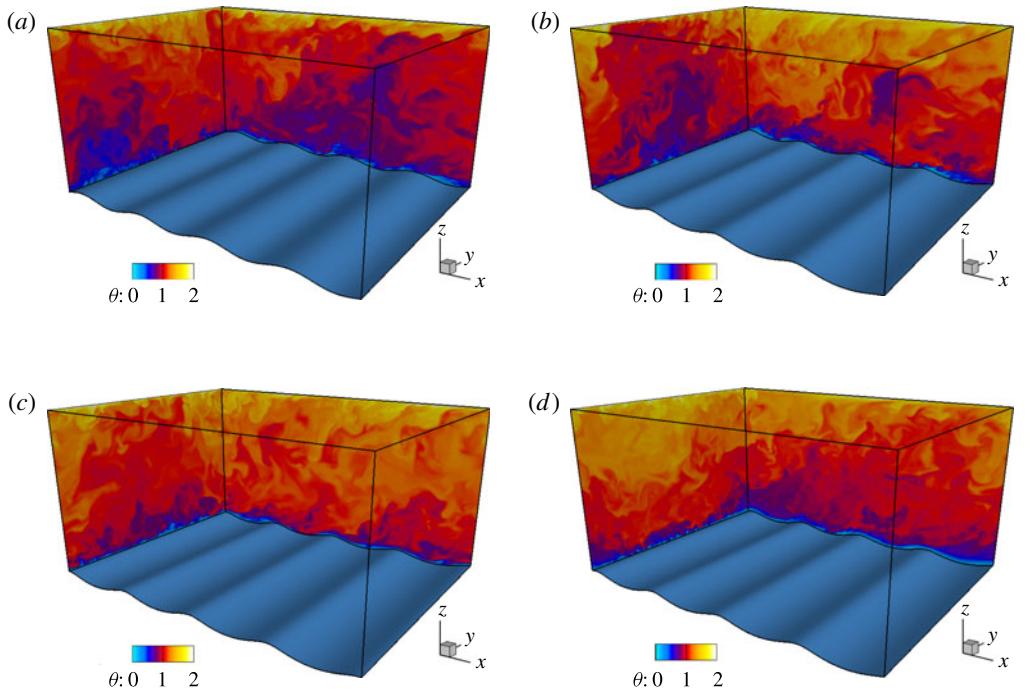


FIGURE 2. (Colour online) Three-dimensional illustration of instantaneous scalar field in turbulence over surface waves for various wave cases: (*a*) S25 (stationary wave); (*b*) W25C2 (slow wave); (*c*) W25C14 (intermediate wave); and (*d*) W25C25 (fast wave). For all cases, the contours of the instantaneous scalar concentration θ for $Sc = 1.0$ are shown on the two representative vertical planes. The wave surface is shaded blue for illustrative purposes. In (*b–d*), the waves propagate in the x-direction.

Sullivan *et al.* 2000; Kihara *et al.* 2007; Yang & Shen 2010)

$$f(x, y, z, t) = \langle f\rangle(x, z) + f'(x, y, z, t) = \overline{f}(\zeta) + \widetilde{f}(x, z) + f'(x, y, z, t), \tag{4.1}$$

where $\langle f\rangle$ denotes the phase average, $\overline{f}$ denotes the time and ζ-plane average over all (ξ, ψ, τ) in the computational space (hereinafter simply referred to as the time and plane average), $\widetilde{f}$ denotes the wave-induced variation of f, and f' denotes the instantaneous fluctuation. In particular, the phase average $\langle f\rangle$ is calculated by shifting the instantaneous quantity f to the same phase with respect to the surface wave, then averaging in time and along the spanwise direction, and lastly further averaging among the four streamwise waves (Yang & Shen 2010). The wave-induced variation is then obtained by subtracting from the phase average the time and plane average at the corresponding ζ level in the computational space, i.e. $\widetilde{f}(x, z) = \langle f\rangle(x, z) - \overline{f}(\zeta)$. As a result of the averaging among the four different waves, only one wavelength is necessary when presenting $\langle f\rangle$ and $\widetilde{f}$. Moreover, when presenting the vertical profile of the time and plane average $\overline{f}$, the ζ coordinate is converted to the physical coordinate above the wave surface as $\overline{z} = \overline{H}\zeta$ (for a flat-surface case, $\overline{z} = z$). Hereinafter, for simplification $\overline{f}$ is also referred to as the mean of f.

Note that to calculate the mean, one could also choose to first interpolate the physical quantities obtained from the boundary-fitted DNS to a regular Cartesian

https://doi.org/10.1017/jfm.2017.164 Published online by Cambridge University Press

grid and then average on planes of constant z. However, by doing so the flow region below the height of the wave crest would be excluded (e.g. Rutgersson & Sullivan 2005). As shown in the following subsections, because the current DNS uses boundary-fitted grid with the ζ-plane nearly parallel to the wave surface near the lower boundary (see figure 29*a* in appendix B), calculating $\bar{f}$ by averaging on planes of constant ζ allows us to capture the linear profiles of mean velocity and scalar in the thin viscous sublayer very close to the wave surface. Meanwhile, in the log-law region the difference of the mean profiles obtained by averaging on z planes and ζ planes is found to be small because the ζ plane becomes flatter as ζ increases (see more information in appendix B). Moreover, defining and calculating $\bar{f}$ based on ζ allows us to have meaningful values for the wave-correlated variation $\tilde{f}$ in the entire phase-averaged domain, including the region above the trough but below the elevation of the crest. Similar triple decomposition approaches as (4.1) have been used in previous studies of turbulent flows over waves (e.g. Sullivan *et al.* 2000; Sullivan & McWilliams 2002; Kihara *et al.* 2007; Hara & Sullivan 2015).

Figure 3 shows the phase-averaged streamlines and scalar concentration $\langle\theta\rangle$ for various wave cases. The streamlines are plotted based on the velocity vector $(\langle u\rangle - c, \langle w\rangle)$, representing the mean flow pattern in the wave-following reference frame. In case S25 (figure 3*a*), due to the large amplitude of the stationary wavy surface, the phase-averaged flow separates on the leeward face of the crest and reattaches on the windward face of the succeeding crest. The streamlines in the separation zone exhibit a closed-circle pattern, which does not extend vertically beyond the elevation of the wave crest. Above the separation zone, the streamlines are nearly horizontal, with a slightly concave curvature above the reattachment region. The distribution of the phase-averaged scalar concentration $\langle\theta\rangle$ exhibits correlation with the streamline patterns (figure 3*b*). Near the wavy surface, the low-$\langle\theta\rangle$ region is lifted up in the separation zone between the crest and the succeeding trough (i.e. roughly between $x/\lambda = 0.1$ and 0.5) due to the mean upward flow motion associated with the separation, resulting in a reduced vertical gradient for $\langle\theta\rangle$; near the reattachment zone (i.e. around $x/\lambda = 0.7$), the mean flow sweeps towards the windward face of the succeeding crest, resulting in a strong near-surface shear layer (from $x/\lambda = 0.6$ to 1.0) with a high vertical gradient for both $\langle u\rangle$ and $\langle\theta\rangle$. These wave-phase-dependent modulations of the near-surface distribution of $\langle\theta\rangle$ are revisited when the Sherwood number Sh is discussed in the next section (§ 4.2). Above the elevation of the crest, the contour lines of $\langle\theta\rangle$ become nearly horizontal, consistent with the horizontal streamlines at these high elevations. Similar near-surface modulation of $\langle\theta\rangle$ has also been reported in the DNS study by Rossi (2010) for transport of a scalar with $Sc = 0.7$ in a turbulent channel flow over a stationary wavy surface with steepness $ak = 0.314$. Figure 4 shows a corresponding case obtained from our DNS (with $ak = 0.314$ and $Re_* = 283$), which yields reasonably good agreement with the DNS results from Rossi (2010).

In case W25C2 (figure 3*c*,*d*), the wave surface has non-zero orbital velocities (u_s, w_s) that induce additional distortion to the flow field above it (in addition to the boundary curvature effect as in case S25). In the reference frame that moves with the wave at its phase speed c, near the surface the mean streamwise velocity $\langle u\rangle - c$ is in the $-x$-direction. As $\langle u\rangle$ increases with height, $\langle u\rangle - c$ becomes zero at the height indicated by the dash-dot line in figure 3(*c*), and becomes positive further above. The layer where $\langle u\rangle - c = 0$, known as the 'critical layer', was found to play a crucial role in the momentum transfer between the turbulence and the surface waves (e.g. Miles 1957; Lighthill 1962; Sullivan *et al.* 2000; Hristov *et al.* 2003). Around the critical layer, the streamlines form a closed-circle pattern, named as the

https://doi.org/10.1017/jfm.2017.164 Published online by Cambridge University Press

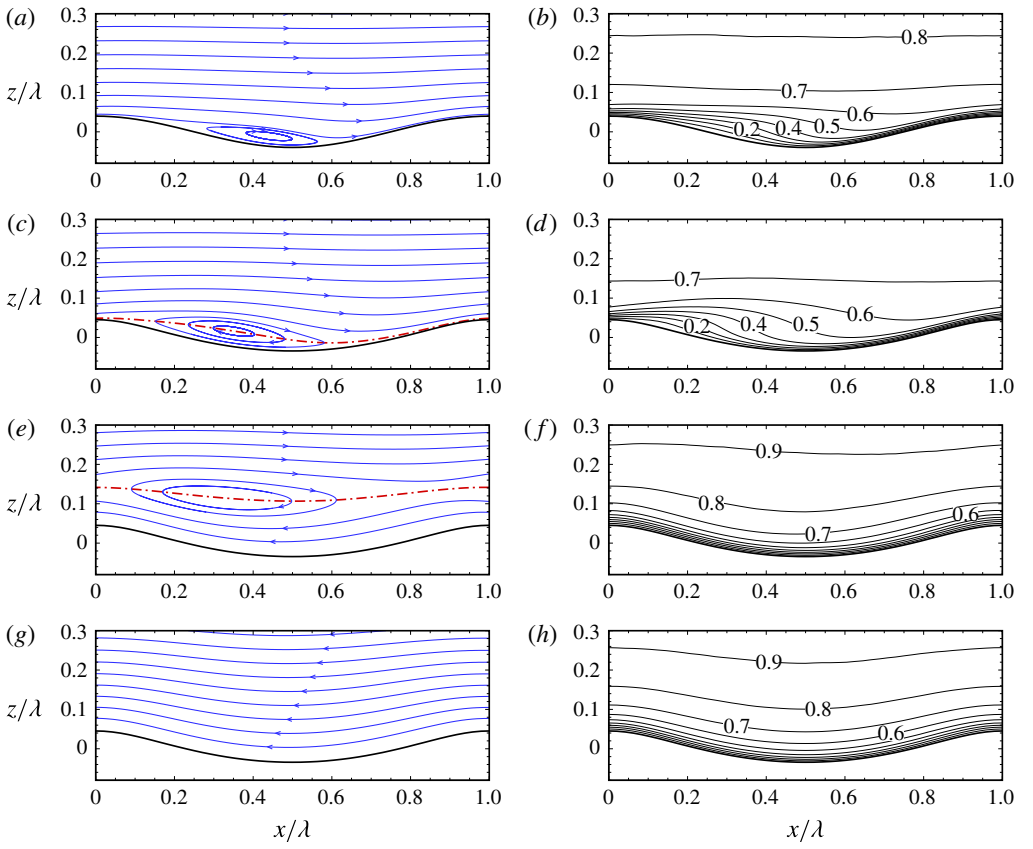


FIGURE 3. (Colour online) Phase-averaged (*a*,*c*,*e*,*g*) streamlines and (*b*,*d*,*f*,*h*) scalar concentration $\langle\theta\rangle$ (for $Sc = 1.0$) for various wave cases: (*a*,*b*) S25; (*c*,*d*) W25C2; (*e*,*f*) W25C14; and (*g*,*h*) W25C25. The streamlines are based on $(\langle u\rangle - c, \langle w\rangle)$, i.e. in the reference frame moving with the wave phase speed c. The red dash-dot line indicates the location of the critical layer where $\langle u\rangle - c = 0$ (it is located higher than $z/\lambda = 0.3$ in case W25C25 and thus is not shown in (*g*)). The contour interval for $\langle\theta\rangle$ is 0.1.

'cat's eye' by Lighthill (1962). For case W25C2, the cat's-eye streamlines are located right above the wave trough. Note that the cat's eyes pattern in figure 3(*c*) does not imply the occurrence of mean flow separation above the wave trough (see Banner & Melville 1976; Gent & Taylor 1977). Unlike in the flow over a stationary wave, in which a negative surface stress (i.e. reversed near-surface flow) would indicate a flow separation, in flows over progressive waves the near-surface flow is in the reversed direction in the wave-following reference frame everywhere above the wave surface. Yang & Shen (2010) used the local relative velocity (with respect to the local surface orbital velocity) and found occasional instantaneous flow separations occur on the leeward face of slow progressive waves, while the mean flow was found to remain unseparated. Similarly, in case W25C2 of the current DNS the mean flow is found to be unseparated. Compared with the mean flow separation bubble in case S25, in case W25C2 the cat's-eye streamline pattern extends further upwards and upstream, As a result, the low-$\langle\theta\rangle$ region above the wave trough is lifted further upwards, and this effect also extends further upstream when compared with case S25.

https://doi.org/10.1017/jfm.2017.164 Published online by Cambridge University Press

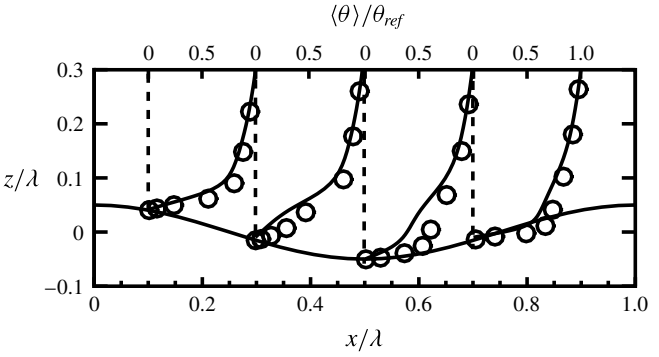


FIGURE 4. Comparison of phase-averaged scalar concentration $\langle\theta\rangle$ with $Sc = 0.7$ over a stationary wavy wall with steepness $ak = 0.314$. Profiles of $\langle\theta\rangle$ at $x/\lambda = 0.1$, 0.3, 0.5, and 0.7 are plotted: ∘, DNS of channel flow by Rossi (2010);——, current DNS with $Re_* = 283$. The reference value θ_{ref} for the normalization is based on the mean scalar concentration at $z = 0.3\lambda$.

For cases W25C14 (figure 3*e*,*f*) and W25C25 (figure 3*g*,*h*), the wave phase speed c is large and the critical layer is located far from the wave surface. Below the critical layer, the streamlines are nearly parallel to the wave surface with the mean streamwise velocity $\langle u\rangle - c$ in the $-x$-direction. Associated with this smooth streamline pattern, the contour lines for $\langle\theta\rangle$ are also nearly parallel to the wave surface. In cases W25C14 and W25C25 the scalar concentration $\langle\theta\rangle$ near the wave surface is in general higher than that in cases S25 and W25C2, as indicated by the lower elevations of the $\langle\theta\rangle = 0.6$ and 0.8 contour lines, respectively, in figures 3(*f*) and 3(*h*) compared with those in figures 3(*b*) and 3(*d*).

The effect of surface waves on the scalar field can be directly visualized from the distribution of the wave-induced variation of the scalar concentration, $\widetilde{\theta}$, in which the time and plane average $\overline{\theta}$ has been removed. Figure 5 shows the two-dimensional contours of $\widetilde{\theta}$ and the vertical profile of the ξ-average of its magnitude, $\overline{|\widetilde{\theta}|}$. For cases S25 (figure 5*a*) and W25C2 (figure 5*b*), the distribution of $\widetilde{\theta}$ is asymmetric about the wave crest, with negative values above the leeward face and trough, and positive values above the windward face and crest. For cases W25C14 (figure 5*c*) and W25C25 (figure 5*d*), the distribution of $\widetilde{\theta}$ becomes nearly symmetric with respect to the wave trough, with positive values above the trough and negative values above the crest. For all the four wave cases, the averaged magnitude $\overline{|\widetilde{\theta}|}$ has its maximum near the wave surface (at $\zeta/\lambda \lesssim 0.04$), and reduces to a small value at higher height. The peak values of $\overline{|\widetilde{\theta}|}$ for cases S25 and W25C2 are significantly higher than those for cases W25C14 and W25C25. Figure 5 also shows the effect of Sc on $\overline{|\widetilde{\theta}|}$. For all of the cases, the increase of Sc causes an increase of the peak value and a reduction in the height of the peak.

4.2. *Sherwood number*

The wave-induced variation of the near-surface scalar field causes considerable wave-correlated variation in the Sherwood number. The Sherwood number is usually used to measure the relative importance of convection and molecular diffusion in convective

https://doi.org/10.1017/jfm.2017.164 Published online by Cambridge University Press

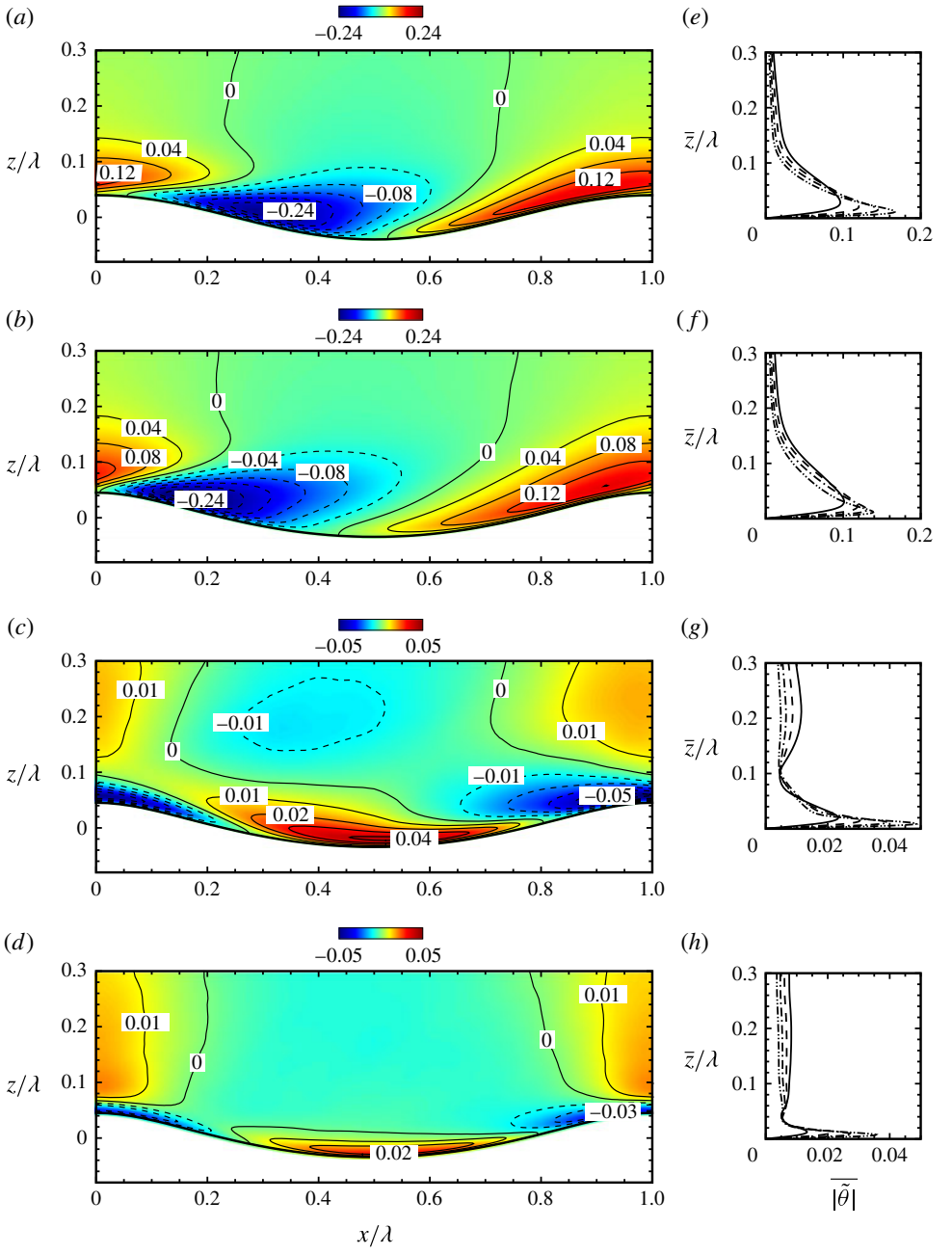


FIGURE 5. (Colour online) Distribution of wave-induced variation of scalar concentration, $\widetilde{\theta}$, for various wave cases: (*a*,*e*) S25; (*b*,*f*) W25C2; (*c*,*g*) W25C14; and (*d*,*h*) W25C25. (*a–d*) Show the contours of $\widetilde{\theta}$ for $Sc = 1.0$. The contour intervals are (*a*,*e*) 0.04, (*b*,*f*) 0.04, (*c*,*g*) 0.01 and (*d*,*h*) 0.01. Dashed contour lines indicate negative values. (*e–h*) Show the vertical profiles of $\overline{|\widetilde{\theta}|}$ (i.e. the average of $|\widetilde{\theta}|$ over all ξ) for various values of Sc: ——, $Sc = 0.5$; – – –, $Sc = 1.0$; — · —, $Sc = 2.0$; and — · · —, $Sc = 4.0$.

https://doi.org/10.1017/jfm.2017.164 Published online by Cambridge University Press

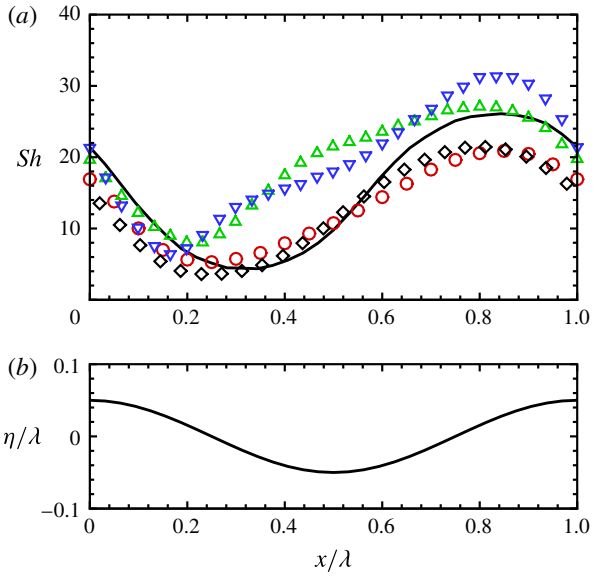


FIGURE 6. (Colour online) (*a*) Profiles of phase-averaged local Sherwood number *Sh* over the stationary wavy wall: ○, RANS result of Park *et al.* (2004) for $(ak, Sc) = (0.1\pi, 0.7)$; □, RANS result of Dellil *et al.* (2004) for $(ak, Sc) = (0.08\pi, 0.9)$; △, RANS result of Dellil *et al.* (2004) for $(ak, Sc) = (0.12\pi, 0.9)$; ▽, LES result of Choi & Suzuki (2005) for $(ak, Sc) = (0.1\pi, 0.7)$; and ——, current DNS result for $(ak, Sc) = (0.1\pi, 0.7)$ and $Re_* = 283$ (see figure 4). The corresponding wave surface phase is indicated by the wave elevation η of $ak = 0.1\pi$ in panel (*b*).

mass transfer processes (corresponding to the Nusselt number in heat transfer). The local Sherwood number along the wave surface based on the phase-averaged scalar field can be calculated as

$$Sh \equiv \frac{h\overline{H}/2}{D} = \frac{\left.\dfrac{\partial\langle\theta\rangle}{\partial z}\right|_{z=\eta}^{\overline{H}}}{2(\overline{\theta}_{1/2} - \theta_0)}, \tag{4.2}$$

where h is the convective mass transfer coefficient, D is the molecular diffusivity as in (2.3), $\overline{\theta}_{1/2}$ is the averaged θ at the centre height of the domain ($\overline{z} = \overline{H}/2$), and $\theta_0 = 0$ is the imposed bottom surface value of θ as the boundary condition. Figure 6 shows the wave-correlated variation of *Sh* for the steep stationary wave case (i.e. the case with $ak = 0.314$ and $Re_* = 283$ as shown in figure 4), in which the current DNS result is compared with the results from several previous numerical studies (Park *et al.* 2004; Dellil *et al.* 2004; Choi & Suzuki 2005). For the steep stationary wave case, the profile of *Sh* has a nearly sinusoidal shape. On the stationary wavy surface, the value of *Sh* is small above the leeward face and large above the windward face, as a result of the smaller and larger vertical gradients of $\langle\theta\rangle$ on the leeward and windward faces, respectively, as shown in figures 3(*a*) and 4.

Figure 7 shows the effect of wave motion on *Sh*. The plotted curves are for $Sc = 1.0$. When the wave is slow (case W25C2), similar to the stationary wave condition, *Sh* is also small above the leeward face and large above the windward face. However, the

https://doi.org/10.1017/jfm.2017.164 Published online by Cambridge University Press

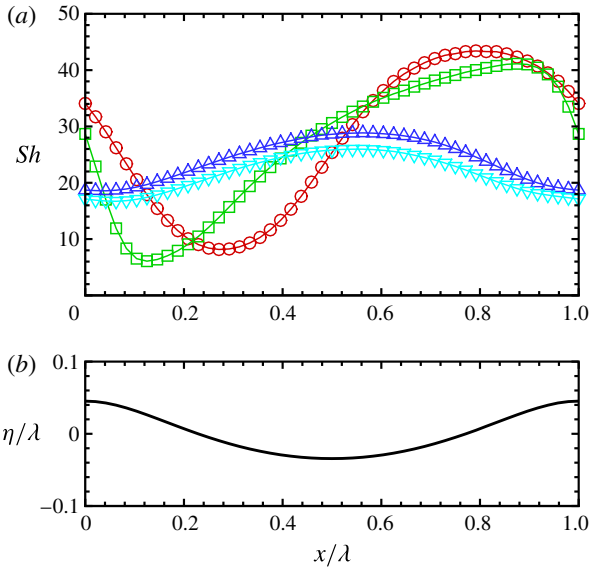


FIGURE 7. (Colour online) (*a*) Profiles of phase-averaged local Sherwood number Sh for $Sc = 1.0$ and for various wave cases: ○, S25 ($c/u_* = 0$); □, W25C2 ($c/u_* = 2$); △, W25C14 ($c/u_* = 14$); and ▽, W25C25 ($c/u_* = 25$). The corresponding wave surface phase is indicated by the wave elevation η in panel (*b*).

shape of the Sh curve apparently differs from the sinusoidal shape, with its minimum point closer to the wave crest (near $x/\lambda = 0.12$). For cases with intermediate (case W25C14) and fast (W25C25) waves, the distribution of Sh become symmetric with respect to the wave form, with the maxima above the wave trough and the minima above the crest, corresponding to the regions of positive and negative $\widetilde{\theta}$ in figure 5, respectively.

For a given wave condition, varying the Sc value mainly causes changes in the magnitudes of the mean and variation of Sh, while the shapes of the curves are similar to those of the corresponding curves shown in figure 7. Thus, these additional Sh curves with different Sc are not plotted here, and only the effect of Sc on the averaged Sherwood number $\overline{Sh}$ $(= (1/\lambda)\int_0^\lambda Sh(x)\mathrm{d}x)$ is discussed. Figure 8 shows the dependence of $\overline{Sh}$ on Sc. Previous studies on scalar transport in wall-bounded or free-surface-bounded turbulent flows have shown that the scaling of $\overline{Sh}$ with Sc follows a power law (e.g. Shaw & Hanratty 1977; Jähne & Haußecker 1998; Na, Papavassiliou & Hanratty 1999; Hasegawa & Kasagi 2008), i.e.

$$\overline{Sh} = \alpha Sc^{\beta}. \tag{4.3}$$

The current DNS results also exhibit this power-law trend for each wave condition as shown in figure 8. For the four different surface wave conditions considered in this study, the power-law coefficient β varies slightly around an averaged value of 0.555, while α varies between 21.13 and 27.09. The pronounced variation of α with the surface wave condition indicates the importance of wave motion on the magnitude of scalar transport. To further elucidate the effect of wave motion on scalar transport, the averaged Sherwood number $\overline{Sh}$ is plotted in figure 9 as a function of the wave

https://doi.org/10.1017/jfm.2017.164 Published online by Cambridge University Press

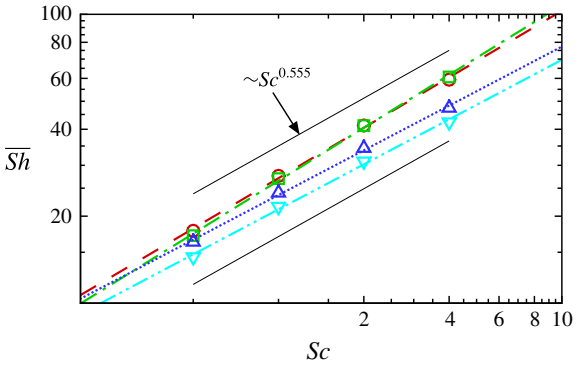


FIGURE 8. (Colour online) Dependence of mean Sherwood number $\overline{Sh}$ on Sc for various wave cases: ○, S25 ($c/u_* = 0$); □, W25C2 ($c/u_* = 2$); △, W25C14 ($c/u_* = 14$); and ▽, W25C25 ($c/u_* = 25$). The lines are the curve fittings: – – –, $\overline{Sh} = 27.09Sc^{0.579}$ for S25; — · —, $\overline{Sh} = 26.54Sc^{0.609}$ for W25C2; · · · , $\overline{Sh} = 23.68Sc^{0.514}$ for W25C14; and — · · —, $\overline{Sh} = 21.13Sc^{0.518}$ for W25C25. The two solid lines show the averaged slope of the four surface wave conditions, i.e. $\overline{Sh} \propto Sc^{0.555}$.

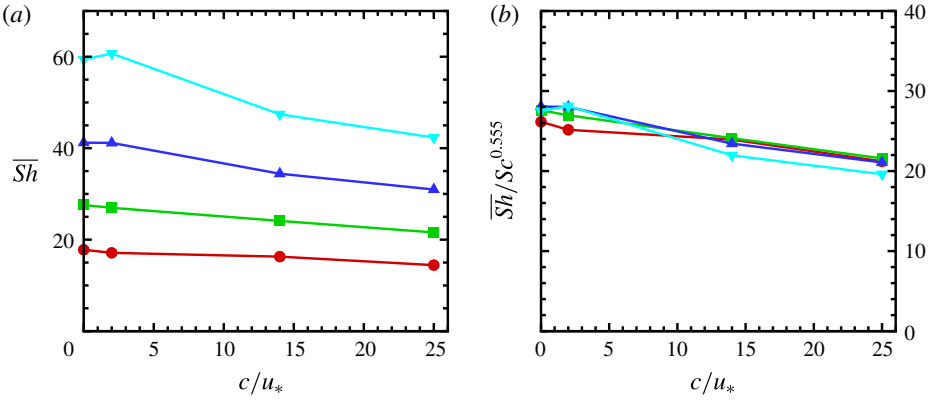


FIGURE 9. (Colour online) Dependence of mean Sherwood number $\overline{Sh}$ on wave age c/u_* for various Schmidt numbers: –●–, $Sc = 0.5$; –■–, $Sc = 1.0$; –▲–, $Sc = 2.0$; and –▼–, $Sc = 4.0$. In panel (*b*), $\overline{Sh}$ is rescaled by $Sc^{0.555}$.

age c/u_*. When Sc is fixed, in general $\overline{Sh}$ decreases as c/u_* increases (figure 9*a*). When normalized by $Sc^{0.555}$ (as suggested by the curve fitting in figure 8), the $\overline{Sh}$ curves for all the different Schmidt numbers collapse reasonably well.

4.3. *Profiles of time- and plane-averaged quantities*

The phase-averaged statistics in § 4.1 have shown significant wave-induced variation in the scalar field, which is highly dependent on the wave phase. In many practical applications, the surface wave effect is usually not directly captured in a phase-resolved context. Instead, the averaged wave effect is parameterized as the effective wave roughness that appears in the one-dimensional profiles of the time- and plane-averaged velocity and scalar concentration, which can be obtained based on field and laboratory measurement data (e.g. Charnock 1955; Smith 1988;

https://doi.org/10.1017/jfm.2017.164 Published online by Cambridge University Press

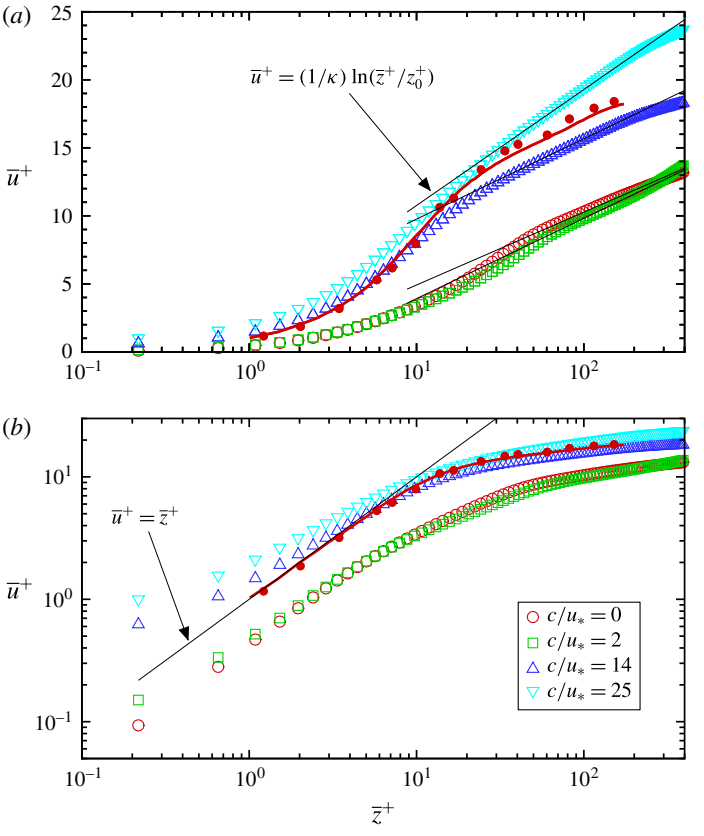


FIGURE 10. (Colour online) Profiles of mean streamwise velocity $\overline{u}^+$ for various wave cases: ○, S25 ($c/u_* = 0$); □, W25C2 ($c/u_* = 2$); △, W25C14 ($c/u_* = 14$); and ▽, W25C25 ($c/u_* = 25$). The semi-logarithmic plot in panel (*a*) highlights the log-law region, with the thin solid lines indicating the logarithmic law $\overline{u}^+ = (1/\kappa)\ln(\overline{z}^+/z_0^+)$ and the corresponding values of κ and z_0^+ for each simulation case given in table 1. The logarithmic plot in panel (*b*) highlights the near-wall viscous layer, with the thin solid lines indicating the linear law $\overline{u}^+ = \overline{z}^+$. In the figure, the DNS result of flat-boundary channel flow from Kim, Moin & Moser (1987) is indicated by the thick line, and the experimental data from Eckelmann (1974) (corrected by Kim *et al.* 1987) are indicated by the filled circles.

Fairall *et al.* 1996; Johnson *et al.* 1998; Toba *et al.* 2001). Although limited to low Reynolds number conditions, DNS has been shown to provide valuable insights for understanding the dependence of the effective wave roughness on the characteristics of the waves (Sullivan *et al.* 2000). In this subsection, time and plane averaging is performed for the instantaneous snapshots of scalar and velocity fields obtained from the current DNS to help quantify the averaged wave effect. Note that the plane average is performed on the ζ-plane in the computational space, as defined in § 4.1.

Figure 10 shows the profiles of the mean streamwise velocity $\overline{u}$ (for the definition, see (4.1) and the associated discussion). The slow wave case (W25C2, $c/u_* = 2$) shows a mean velocity profile close to that of the stationary wave case (S25). As c/u_* increases, the profile of $\overline{u}^+$ shifts monotonically towards higher values, which is expected since the wave form drag decreases as c/u_* increases (Belcher & Hunt 1998). For the current DNS, the normalized pressure-induced form drag F_p and surface

https://doi.org/10.1017/jfm.2017.164 Published online by Cambridge University Press

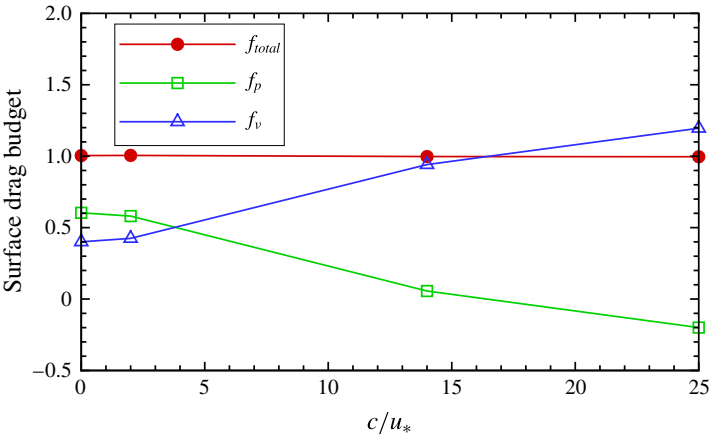


FIGURE 11. (Colour online) Budget of surface drag as a function of wave age: —●—, total surface drag f_{total};—□—, pressure-induced form drag f_p; and —△—, viscous drag f_v.

viscous drag F_v per unit projected horizontal area can be calculated based on the phase-averaged pressure and velocity as

$$F_p = \frac{1}{u_*^2 \lambda} \int_0^\lambda \frac{\langle p \rangle}{\rho} \frac{\partial \eta}{\partial x} \, \mathrm{d}x, \tag{4.4}$$

$$F_v = \frac{1}{u_*^2 \lambda} \int_0^\lambda \nu \left[\left(\frac{\partial \langle u \rangle}{\partial z} + \frac{\partial \langle w \rangle}{\partial x} \right) - 2 \frac{\partial \langle u \rangle}{\partial x} \frac{\partial \eta}{\partial x} \right] \mathrm{d}x, \tag{4.5}$$

and the total surface drag per unit area equals to their sum, $F_{total} = F_p + F_v$. As shown in figure 11, in cases S25 and W25C2, the form drag makes a significant contribution to the total surface drag. In case W25C14, the form drag is very small and the total surface drag is mostly due to the viscous effect, indicating that the mean flow and the surface wave are nearly in equilibrium. In case W25C25, the wave phase speed is fast and the surface wave pushes the mean flow forwards, resulting in negative form drag (i.e. a thrust). A similar dependence of the surface drag on the wave age has been reported in various previous studies (e.g. Li *et al.* 2000; Sullivan *et al.* 2000; Kihara *et al.* 2007; Yang & Shen 2010).

For all the four wave conditions considered in this study, the mean velocity profiles exhibit a distinct logarithmic region, as indicated by the thin solid lines in the semi-logarithmic plot in figure 10(*a*). These lines are determined by fitting the mean velocity profiles in the range of $\overline{z}^+ \in [50, 150]$ (see appendix B) with the logarithmic profile

$$\overline{u}^+ = \frac{1}{\kappa} \ln \left(\overline{z}^+ / z_0^+ \right) = \frac{1}{\kappa} \ln(\overline{z}^+) + B, \tag{4.6}$$

where the superscript '+' denotes the quantities normalized by the wall units (i.e. velocity is normalized by u_* and length is normalized by ν/u_*), κ is the von Kármán constant, z_0^+ is the effective wave surface roughness, and B is the profile offset. For each case, the corresponding log-law profile parameters κ, z_0^+ and B are listed in table 1. Similar to the DNS results reported in Sullivan *et al.* (2000), the evaluated z_0^+ values in most of the DNS cases considered in this study fall in the transitional regime ($0.1 < z_0^+ < 2.2$) in terms of the sea-surface roughness, which was

https://doi.org/10.1017/jfm.2017.164 Published online by Cambridge University Press

categorized to be a common sea state by Kitaigorodskii & Donelan (1984). The slow wave case W25C2 exhibits a roughness of $z_0^+ = 2.31$ that is slightly higher than the upper bound of the transitional regime. For cases S25, W25C2 and W25C14, the values for κ are close to the standard value of $\kappa = 0.41$ for the flat-wall case. The fast wave case W25C25 exhibits a smaller value of $\kappa = 0.27$, which is likely due to the strong surface motion of the fast propagating surface waves when $c/u_* = 25$. Similarly, Sullivan *et al.* (2000) reported a 10 % reduction of κ in DNS of turbulence over progressive waves with $ak = 0.1$ (i.e. the waves are less steep than the ones studied here). Note that due to this smaller κ in case W25C25, its evaluated z_0^+ is larger than that in case W25C14. Therefore, the larger z_0^+ in case W25C25 does not imply that the turbulence sees the fast wave 'rougher' than the intermediate wave. It should be pointed out that caution should be taken when interpreting the mean velocity profile for the present fast wave case due to the limited Reynolds number used in this study. Under real oceanic conditions, the fast wave case usually corresponds to the wind over storm-generated ocean swells, for which the Reynolds number is much higher than what a DNS can afford. The current DNS of $c/u_* = 25$ are more relevant to the condition of light wind over fast mechanically generated waves in laboratory-scale wind–wave tanks (e.g. Buckley & Veron 2016). Further study is required in the future in order to understand the effect of surface waves on the von Kármán constant and the wave surface roughness.

The near-surface behaviour of the mean velocity profile is shown by the logarithmic plot in figure 10(*b*). The mean velocity profiles exhibit a nearly linear behaviour in the viscous sublayer (i.e. $\overline{z}^+ < 5$), with some non-negligible difference from the linear law of the flat-wall turbulence. In particular, the viscous sublayer profiles of the intermediate (W25C14) and fast (W25C25) wave cases are close to the linear profile of the flat-wall case (e.g. Kim *et al.* 1987; Lee & Moser 2015), i.e. $\overline{u}^+ = \overline{z}^+$, but with larger value towards the wave surface due to the positive mean streamwise surface orbital velocity of the nonlinear Stokes wave. On the other hand, the stationary (S25) and slow (W25C2) wave cases also show a linear profile in the viscous sublayer, but with a velocity deficit compared with the flat-wall linear law. The viscous sublayer profile of the stationary wave case (S25) is nearly parallel to that of the flat wall, while the one for the slow wave case (W25C2) is tilted slightly towards higher values when approaching the surface due to the positive mean surface orbital velocity of the Stokes waves.

A similar analysis can be done for the mean scalar concentration. By compiling a number of experimental datasets, Kader (1981) showed that the mean temperature and scalar concentration in fully developed turbulent boundary layers follow a linear profile in the viscous sublayer and a logarithmic profile in the log-law region. In the near-surface region, the Kader correlation suggests that

$$\overline{\theta}^+/Sc = \overline{z}^+ - Sc[c_4\overline{z}^{+4} + O(\overline{z}^{+5})], \tag{4.7}$$

where $c_4 \approx 1.5 \times 10^{-4}$ as estimated based on the experimental data (Kader 1981). Therefore, for the flat-wall case it is expected that

$$\overline{\theta}^+ \approx Sc\,\overline{z}^+ \tag{4.8}$$

to the leading order near the surface, with the deviation from this linear profile increasing towards larger $\overline{z}^+$ and with higher Sc. Similar near-surface linear behaviour is found in the current DNS results over wave surfaces. Here $\overline{\theta}^+ = \overline{\theta}/\theta_*$, where

$$\theta_* = \frac{D}{u_*}\frac{\mathrm{d}\overline{\theta}}{\mathrm{d}\overline{z}}\bigg|_{\overline{z}=0} \tag{4.9}$$

https://doi.org/10.1017/jfm.2017.164 Published online by Cambridge University Press

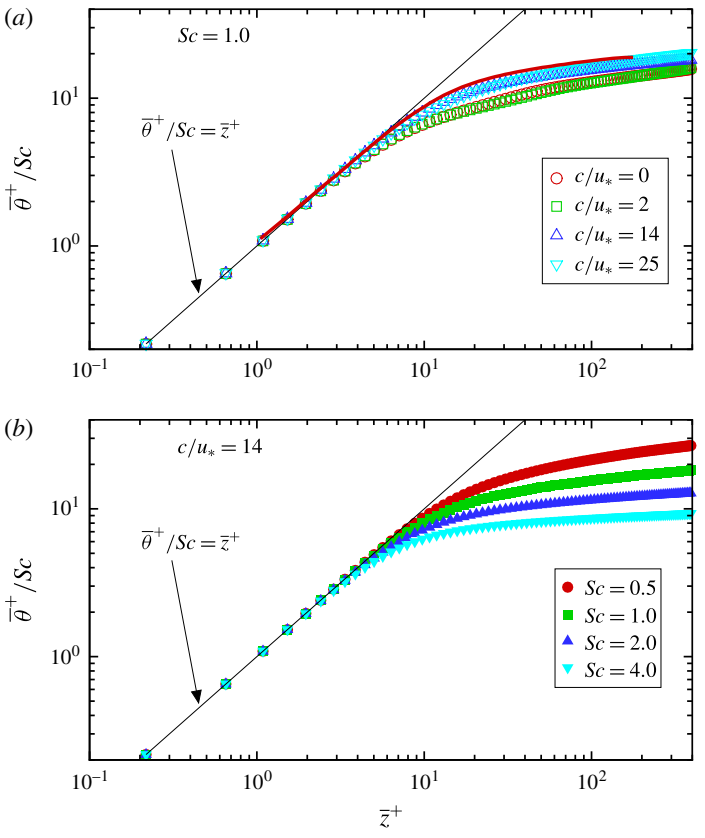


FIGURE 12. (Colour online) Profiles of rescaled mean scalar concentration $\overline{\theta}^+/Sc$. Panel (*a*) shows various wave cases with a fixed Schmidt number $Sc = 1.0$: ○, S25 ($c/u_* = 0$); □, W25C2 ($c/u_* = 2$); △, W25C14 ($c/u_* = 14$); and ▽, W25C25 ($c/u_* = 25$). Panel (*b*) shows case W25C14 ($c/u_* = 14$) with various Schmidt numbers: ●, $Sc = 0.5$; ■, $Sc = 1.0$; ▲, $Sc = 2.0$; and ▼, $Sc = 4.0$. The profiles are shown on a logarithmic scale to highlight the near-wall region, with the solid line indicating the linear law $\overline{\theta}^+/Sc = \overline{z}^+$. In panel (*a*), the DNS result from Kawamura *et al.* (1998) is also plotted (the thick line).

is a characteristic scalar scale (in the case of heat transfer, θ_* is also referred to as the friction temperature) (Kim & Moin 1989). Figure 12 shows the profiles of $\overline{\theta}^+/Sc$ (in a logarithmic plot) for some representative cases obtained by the current DNS. In particular, figure 12(*a*) shows the profiles for various wave cases with $Sc = 1.0$, and figure 12(*b*) shows the profiles for case W25C14 with various Schmidt numbers (other cases also follow consistent trends for the wave and Sc dependences, and are thus not shown here due to space limitation). In the viscous sublayer ($\overline{z}^+ < 5$), the profiles for different wave conditions and Schmidt numbers collapse well and agree with the linear law found in the flat-wall condition.

The logarithmic law behaviour of $\overline{\theta}^+$ can be visualized in a semi-logarithmic plot as shown in figure 13. Similar to the profile of $\overline{u}^+$, for a fixed Sc the $\overline{\theta}^+$ profile shifts towards higher values when c/u_* increases, with the profile for $c/u_* = 2$ close to that for the stationary wave case (figure 13*a*). For each wave condition, the $\overline{\theta}^+$ profile shifts monotonically to higher values when Sc increases (see for example the

https://doi.org/10.1017/jfm.2017.164 Published online by Cambridge University Press

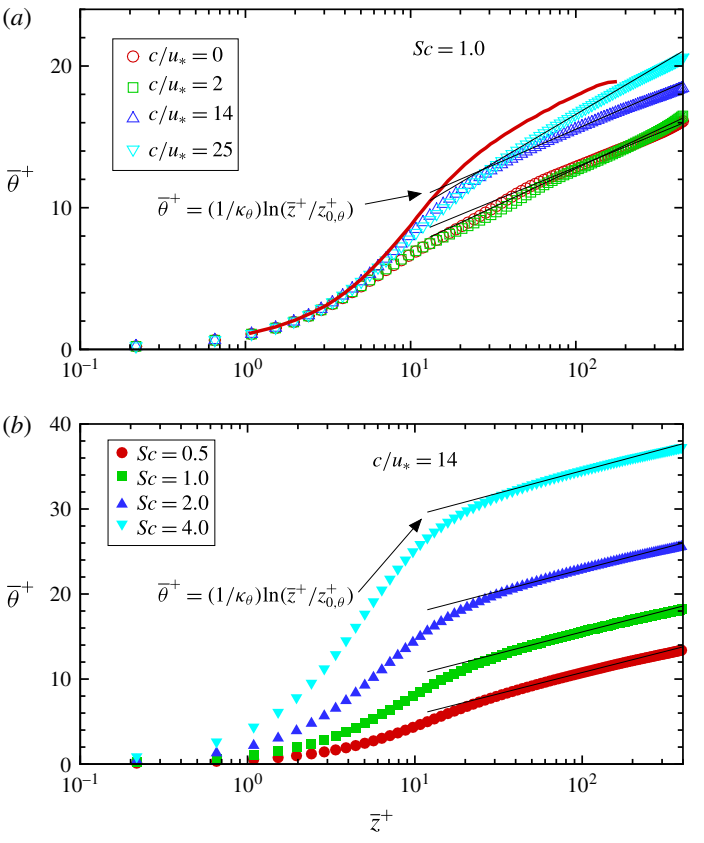


FIGURE 13. (Colour online) Profiles of mean scalar concentration $\overline{\theta}^+$. The definitions of the symbols are the same as those in figure 12. The profiles are shown on a semi-logarithmic scale to highlight the log-law region, with the thin solid lines indicating the logarithmic law $\overline{\theta}^+ = (1/\kappa_\theta)\ln(\overline{z}^+/z^+_{0,\theta})$ and the corresponding values of κ_θ and $z^+_{0,\theta}$ for each simulation case given in table 1. In panel (*a*), the DNS result from Kawamura *et al.* (1998) is also plotted (the thick line).

case W25C14 shown in figure 13*b*). Similar to (4.6), the logarithmic law for scalar concentration can be written as (e.g. Kader 1981)

$$\overline{\theta}^+ = \frac{1}{\kappa_\theta}\ln(\overline{z}^+/z^+_{0,\theta}) = \frac{1}{\kappa_\theta}\ln\overline{z}^+ + B_\theta, \tag{4.10}$$

where κ_θ is the von Kármán constant of scalar, $z^+_{0,\theta}$ is the effective wave surface roughness for scalar, and B_θ is the offset of the mean scalar profile. For each wave case, the corresponding parameters κ_θ, $z^+_{0,\theta}$, and B_θ can be obtained by fitting the DNS data in the log-law region (defined as $50 < z^+ < 150$ in this study as explained in appendix B) with the logarithmic profile (4.10). The estimated values of these parameters are listed in table 1. For each wave case, the evaluated value of the scalar von Kármán constant κ_θ exhibits a small variation when the Schmidt number is changed, while the profile offset B_θ (or the roughness $z^+_{0,\theta}$) increases significantly as Sc increases.

https://doi.org/10.1017/jfm.2017.164 Published online by Cambridge University Press

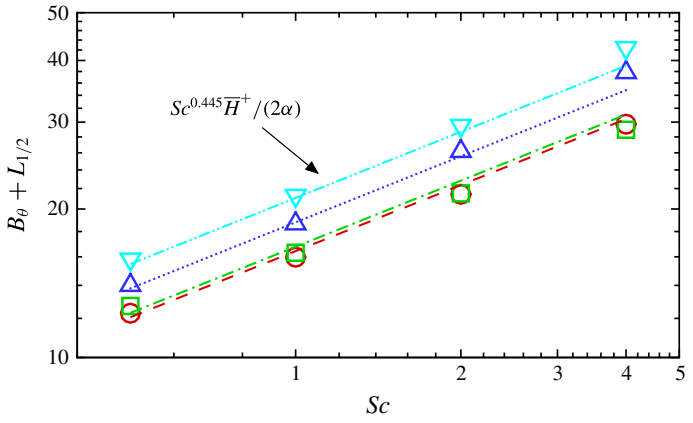


FIGURE 14. (Colour online) Dependence of B_θ on the Schmidt number for various wave cases: ○, S25 ($c/u_* = 0$); □, W25C2 ($c/u_* = 2$); △, W25C14 ($c/u_* = 14$); and ▽, W25C25 ($c/u_* = 25$). Equation (4.14) suggests that $B_\theta + L_{1/2} = Sc^{1-\beta}\overline{H}^+/(2\alpha)$, as shown by the lines: – – –, S25; — · —, W25C2; · · · , W25C14; and — · · —, W25C25. For the current DNS, $\beta \approx 0.555$ when averaged among the four wave conditions, and the α value for each wave condition can be found in the caption of figure 8.

The dependence of B_θ on Sc can be further quantified. Recall that the averaged Sherwood number $\overline{Sh}$ follows a power-law dependence on Sc, as shown in (4.3). Applying the surface average to (4.2) and combining it with (4.3) yields

$$\alpha Sc^{\beta} = \left.\frac{\mathrm{d}\overline{\theta}^+}{\mathrm{d}\overline{z}}\right|_{\overline{z}^+=0} \frac{\overline{H}^+}{2\overline{\theta}^+_{1/2}}. \tag{4.11}$$

The near-surface linear profile (4.8) gives

$$\left.\frac{\mathrm{d}\overline{\theta}^+}{\mathrm{d}\overline{z}}\right|_{\overline{z}^+=0} = Sc, \tag{4.12}$$

and the logarithmic profile (4.10) gives

$$\overline{\theta}^+_{1/2} = \frac{1}{\kappa_\theta}\ln\left(\overline{H}^+/2\right) + B_\theta. \tag{4.13}$$

Substituting (4.12) and (4.13) into (4.11) gives

$$B_\theta = \frac{\overline{H}^+}{2\alpha}Sc^{1-\beta} - L_{1/2}, \tag{4.14}$$

where

$$L_{1/2} = \frac{1}{\kappa_\theta}\ln\left(\overline{H}^+/2\right). \tag{4.15}$$

As shown in table 1 and figure 9, for a given wave condition the parameters α, β and κ_θ estimated based on the current DNS data are nearly constant. Therefore, equation (4.14) suggests that $B_\theta \sim Sc^{1-\beta}$, where $\beta \approx 0.555$ as shown in § 4.2. Figure 14 shows the estimated $B_\theta + L_{1/2}$ as a function of the Schmidt number. With $\beta = 0.555$ and α given by the power-law fitting in figure 8, equation (4.14) is found to provide a reasonable parameterization for B_θ, which agrees well with the B_θ values obtained directly from the log-law profile fitting (the values are listed in table 1).

https://doi.org/10.1017/jfm.2017.164 Published online by Cambridge University Press

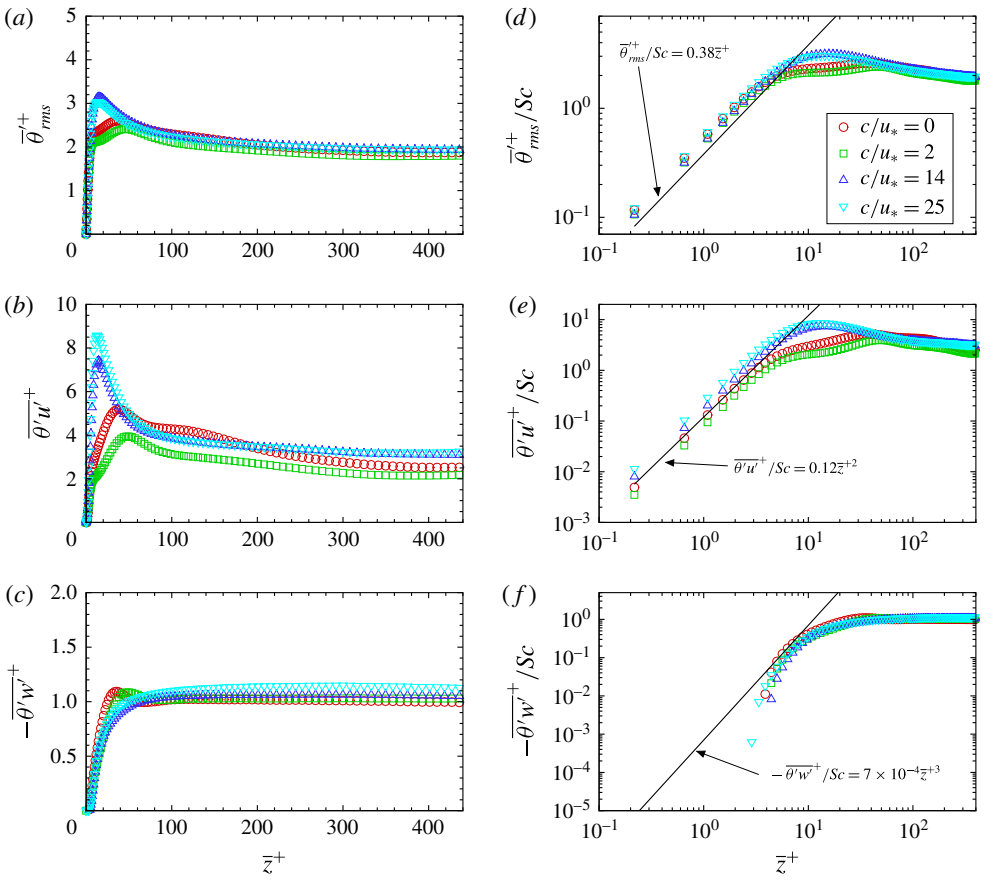


FIGURE 15. (Colour online) Profiles of (*a*) $\overline{\theta'}^+_{rms}$, (*b*) $\overline{\theta'u'}^+$, and (*c*) $\overline{-\theta'w'}^+$ on a linear scale; and profiles of (*d*) θ'^+_{rms}/Sc, (*e*) $\overline{\theta'u'}^+/Sc$, and (*f*) $\overline{-\theta'w'}^+/Sc$ on a logarithmic scale. The plotted DNS results are for $Sc = 1.0$ with various wave cases: ○, S25 ($c/u_* = 0$); □, W25C2 ($c/u_* = 2$); △, W25C14 ($c/u_* = 14$); and ▽, W25C25 ($c/u_* = 25$). The solid lines in (*d–f*) indicate the expressions proposed by Kawamura *et al.* (1998).

4.4. *Time- and plane-averaged statistics of scalar fluctuations*

The presence of surface waves can induce a strong effect on the air turbulence. Statistics of velocity fluctuations above plane progressive waves of various wave ages and steepnesses have been studied in detail in previous studies (e.g. Sullivan *et al.* 2000; Kihara *et al.* 2007; Sullivan *et al.* 2008; Yang & Shen 2010; Hara & Sullivan 2015). On the other hand, the statistics of scalar fluctuations over waves have rarely been studied, with the exception of some studies for stationary wavy walls (e.g. Dellil *et al.* 2004; Park *et al.* 2004; Rossi 2010) and for stratified turbulence over water waves (e.g. Sullivan & McWilliams 2002; Druzhinin *et al.* 2016).

In this subsection, the time- and plane-averaged statistics of scalar fluctuations are studied based on the DNS data. Figure 15(*a–c*) shows the profiles of $\overline{\theta'}^+_{rms}$, $\overline{\theta'u'}^+$, and $\overline{-\theta'w'}^+$ for various wave cases with $Sc = 1.0$. The profiles of $\overline{\theta'}^+_{rms}$ (figure 15*a*) and $\overline{\theta'u'}^+$ (figure 15*b*) have a similar trend. As $\overline{z}^+$ increases from 0, the value first increases to a peak and then decreases to approach a constant value. In particular,

https://doi.org/10.1017/jfm.2017.164 Published online by Cambridge University Press

the maximum is at $\overline{z}^+ \approx 35$ for case S25, $\overline{z}^+ \approx 47$ for case W25C2, and $\overline{z}^+ \approx 15$ for cases W25C14 and W25C25. Among the three progressive wave cases, the peak values of both $\overline{\theta}^+_{rms}$ and $\overline{\theta' u'}^+$ increase with c/u_*, indicating the increase of wave effect as the wave propagates faster. The peak values of $\overline{\theta}^+_{rms}$ and $\overline{\theta' u'}^+$ in case S25 are slightly higher than the corresponding ones in case W25C2, because the presence of flow separation in case S25 (figure 3*a*) enhances the turbulence intensity above the wave trough. The wave-induced effect on $\overline{\theta}^+_{rms}$ and $\overline{\theta' u'}^+$ appears to be mainly in the viscous wall region (i.e. $\overline{z}^+ < 50$), with only slight differences at higher elevation.

Figure 15(*c*) shows the profiles of $\overline{-\theta' w'}^+$. Assuming a statistically steady state and integrating the scalar transport equation over a control volume, the total vertical scalar flux at any height z,

$$\overline{-\theta' w'} + D\frac{\mathrm{d}\overline{\theta}}{\mathrm{d}\overline{z}} = \theta_* u_*, \tag{4.16}$$

is a constant in the stress-driven Couette flow considered in the present study. In the viscous wall region ($\overline{z}^+ < 50$), the contribution from the molecular flux $D\mathrm{d}\overline{\theta}/\mathrm{d}\overline{z}$ is significant, therefore the value of $\overline{-\theta' w'}^+$ ($= \overline{-\theta' w'}/\theta_* u_*$) is less than 1. In this region, the values of $\overline{-\theta' w'}^+$ in cases S25 and W25C2 are larger than those in cases W25C14 and W25C25. In the outer region ($\overline{z}^+ > 50$), the molecular diffusion effect is negligible and thus $\overline{-\theta' w'}^+ \approx 1.0$ for all of the cases. Similar to $\overline{\theta}^+_{rms}$ and $\overline{\theta' u'}^+$, the profile of $\overline{-\theta' w'}^+$ is also affected by the surface waves mainly in the viscous wall region. In particular, as $\overline{z}^+$ increases, $\overline{\theta' u'}^+$ approaches 1 more rapidly in cases S25 and W25C2 than in cases W25C14 and W25C25, indicating more intensive turbulent mixing in cases S25 and W25C2.

Previous studies on scalar transport over flat boundary have shown that in the viscous sublayer (i.e. $\overline{z}^+ < 5$) the scalar fluctuation profiles can be expressed (to the leading order) as (e.g. Antonia & Kim 1991; Kawamura *et al.* 1998)

$$\overline{\theta}^+_{rms}/Sc = 0.38\overline{z}^+, \tag{4.17}$$

$$\overline{\theta' u'}^+/Sc = 0.12\overline{z}^{+2}, \tag{4.18}$$

$$\overline{-\theta' w'}^+/Sc = 7 \times 10^{-4}\overline{z}^{+3}. \tag{4.19}$$

To look closely at the viscous sublayer, we plot in figure 15(*d–f*) the profiles of $\overline{\theta}^+_{rms}/Sc$, $\overline{\theta' u'}^+/Sc$, and $\overline{-\theta' w'}^+/Sc$ on a logarithmic scale. For $\overline{\theta}^+_{rms}/Sc$ and $\overline{\theta' u'}^+/Sc$, the DNS results for various wave cases are found to be close to the expressions given by (4.17) and (4.18), respectively. Differently, for $\overline{-\theta' w'}^+/Sc$ the presence of waves causes an obvious discrepancy from the flat-wall expression given by (4.19). For better understanding of the effect of surface waves on the vertical scalar flux $-\theta' w'$, more turbulence statistics are quantified and discussed later in §§ 4.5 and 4.6.

Figure 16 shows the effect of Sc on the time- and plane-averaged statistics of scalar fluctuation and fluxes. In particular, figure 16(*a–c*) shows the profiles of $\overline{\theta}^+_{rms}$, $\overline{\theta' u'}^+$, and $\overline{-\theta' w'}^+$ for the wave case W25C14 with various Sc. For $\overline{\theta}^+_{rms}$ (figure 16*a*) and $\overline{\theta' u'}^+$ (figure 16*b*), when Sc increases, their peaks in the viscous wall region (i.e. $\overline{z}^+ < 50$) increase significantly, while in the outer layer (i.e. $\overline{z}^+ > 50$) the profiles only slightly shift towards larger values. When rescaled by Sc and plotted on a logarithmic scale, in the viscous sublayer (i.e. $\overline{z}^+ < 5$) the profiles of $\overline{\theta}^+_{rms}/Sc$ (figure 16*d*) and $\overline{\theta' u'}^+/Sc$ (figure 16*e*) for all of the four Sc values are close to the expressions given by (4.17) and (4.18), respectively. Differently, the change of Sc has much less effect on the profile of $\overline{-\theta' w'}^+$ (figure 16*c*). When plotted on a logarithmic scale (figure 16*f*),

https://doi.org/10.1017/jfm.2017.164 Published online by Cambridge University Press

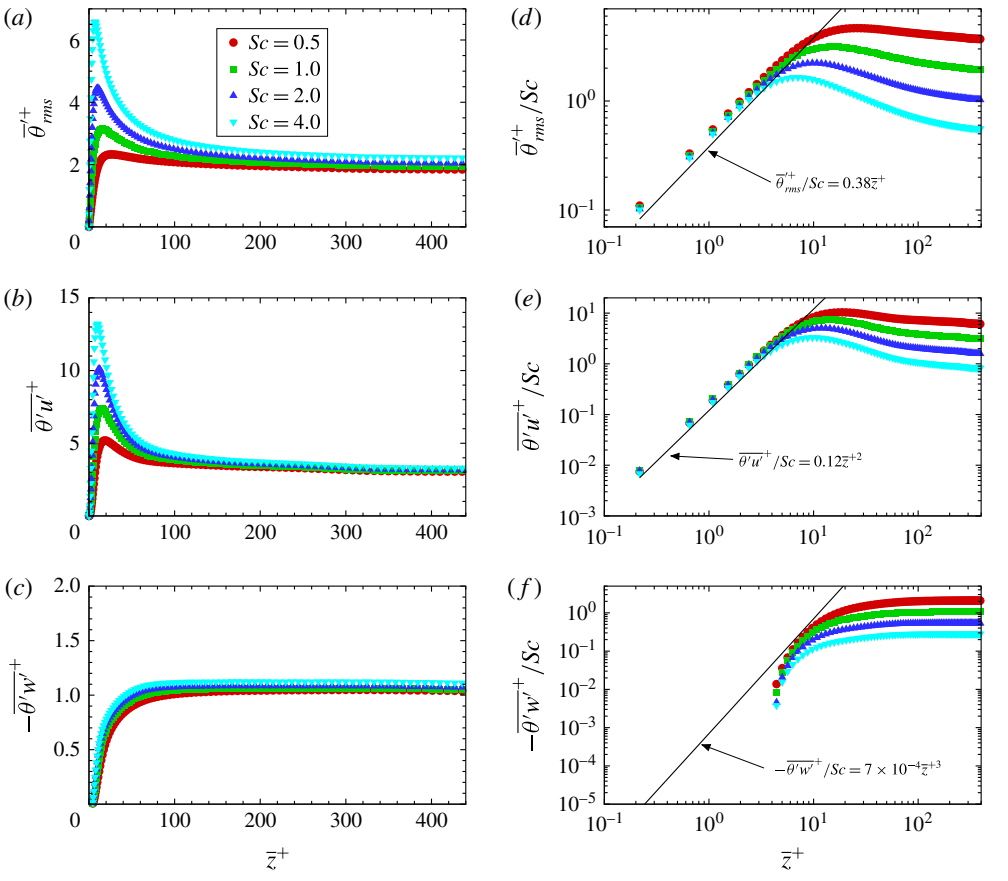


FIGURE 16. (Colour online) Profiles of (*a*) $\overline{\theta}^{+}_{rms}$, (*b*) $\overline{\theta' u'}^{+}$, and (*c*) $\overline{-\theta' w'}^{+}$ on a linear scale; and profiles of (*d*) θ'^{+}_{rms}/Sc, (*e*) $\overline{\theta' u'}^{+}/Sc$, and (*f*) $\overline{-\theta' w'}^{+}/Sc$ on a logarithmic scale. The plotted DNS results are for the wave case W25C14 with various Schmidt numbers: -●-, $Sc = 0.5$; -■-, $Sc = 1.0$; -▲-, $Sc = 2.0$; and -▼-, $Sc = 4.0$. The solid lines in (*d–f*) indicate the expressions proposed by Kawamura *et al.* (1998).

the profiles of $\overline{-\theta' w'}^{+}/Sc$ differ significantly from the flat-wall expression given by (4.19), similar to the results shown in figure 15(*f*).

In figures 15 and 16, only a number of selected cases are shown to illustrate the effect of surface waves and Schmidt number on the statistics of scalar fluctuations. Other cases exhibit similar trends for the surface wave and Sc effects. Note that in the logarithmic plots shown in figures 15(*f*) and 16(*f*), for most of the cases the viscous sublayer portion of the $\overline{-\theta' w'}^{+}/Sc$ profile cannot be displayed because $\overline{-\theta' w'}^{+}/Sc < 0$ there, which is caused by the strong wave-induced modulation to the vertical scalar flux $-\theta' w'$. About this point, more discussions are given in §§ 4.5 and 4.6.

4.5. *Wave-correlated distribution of scalar variance and fluxes*

To help understand the effect of surface waves on the scalar fluctuation statistics, in this subsection the phase averaging method (see § 4.1 for the mathematical definition) is used to quantify the wave-correlated distribution of the scalar variance and fluxes.

https://doi.org/10.1017/jfm.2017.164 Published online by Cambridge University Press

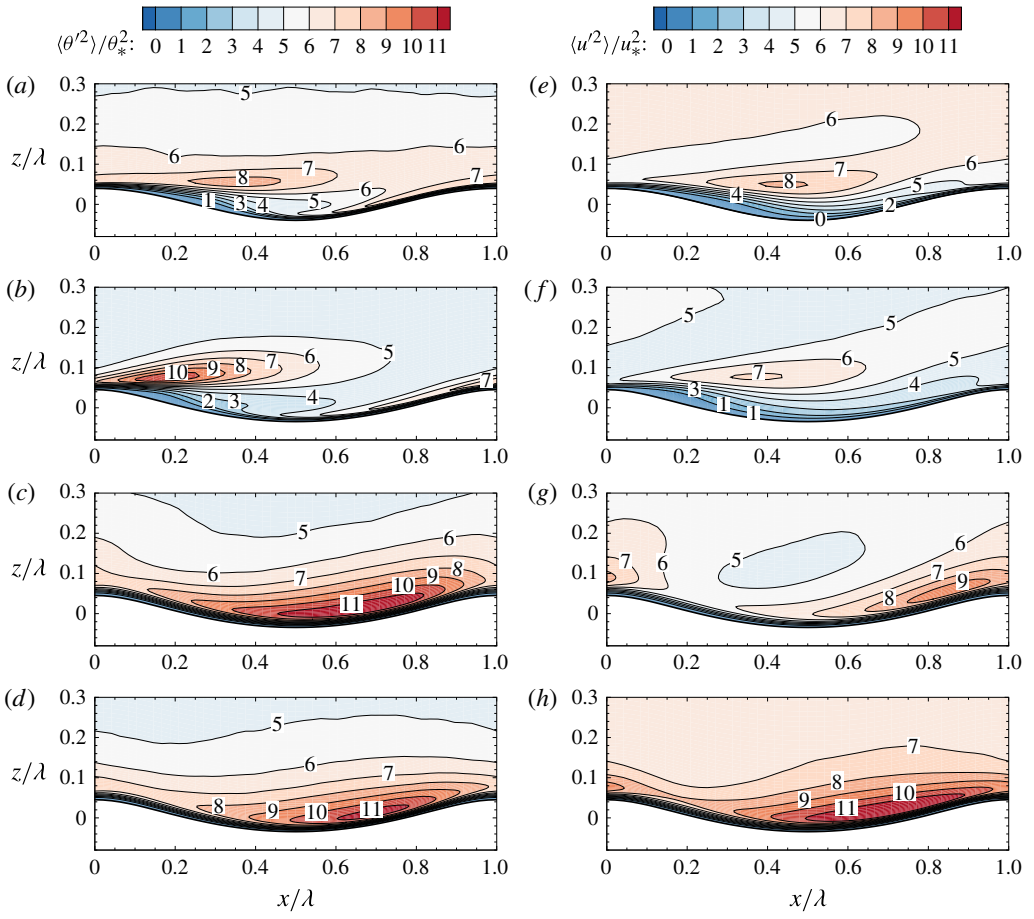


FIGURE 17. (Colour online) Contours of $\langle\theta'^2\rangle/\theta_*^2$ for various wave cases: (*a*) S25; (*b*) W25C2; (*c*) W25C14; and (*d*) W25C25. Contours of $\langle u'^2\rangle/u_*^2$ for various wave cases: (*e*) S25; (*f*) W25C2; (*g*) W25C14; and (*h*) W25C25. $Sc = 1.0$.

In particular, for each wave case the DNS results for $Sc = 1.0$ are presented. The results for other Schmidt numbers exhibit similar wave-correlated behaviours, and are thus not shown here.

Figure 17 shows the contours of the phase-averaged scalar variance, $\langle\theta'^2\rangle$, and the phase-averaged streamwise velocity variance, $\langle u'^2\rangle$. The scalar variance $\langle\theta'^2\rangle$ shows considerable correlation with $\langle u'^2\rangle$, and exhibits strong phase-dependent variation induced by the surface waves. In particular, for the stationary wave case S25 (figure 17*a*,*e*) there exists a strong shear layer with high intensity for $\langle\theta'^2\rangle$ and $\langle u'^2\rangle$, which originates from the crest and extends downstream to above the succeeding trough. In case W25C2 (figure 17*b*), the high-$\langle\theta'^2\rangle$ region is also located above the trough, but the maximum is located more upstream than that in case S25. The high-$\langle\theta'^2\rangle$ regions in cases S25 and W25C2 are consistent with the high vertical gradient regions for $\langle\theta\rangle$ shown in figures 3(*b*) and 3(*d*), respectively.

Different from cases S25 and W25C2, in cases W25C14 and W25C25 the high-$\langle\theta'^2\rangle$ regions are located above the windward face of the wave crest, and are much closer to the surface as a result of the smooth streamlines and $\langle\theta\rangle$ contour lines that are parallel

https://doi.org/10.1017/jfm.2017.164 Published online by Cambridge University Press

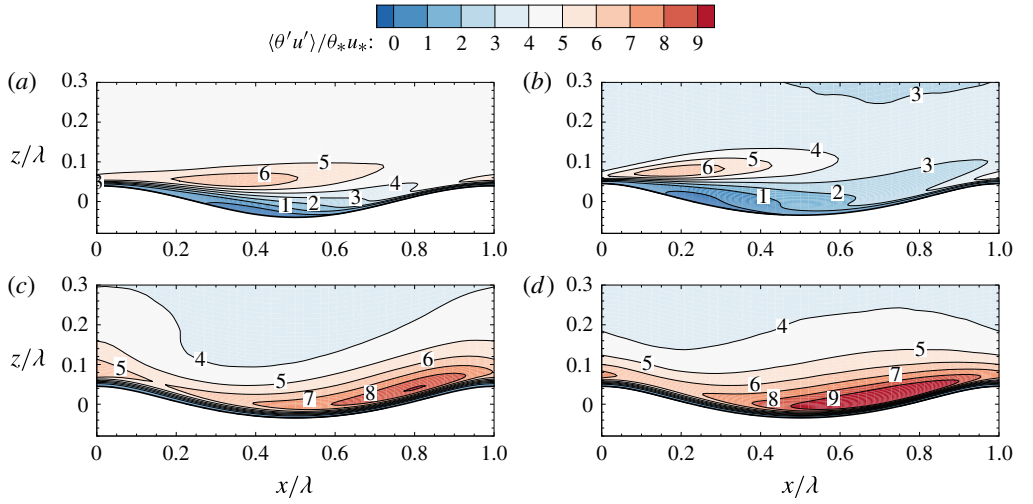


FIGURE 18. (Colour online) Contours of $\langle\theta'u'\rangle/\theta_* u_*$ for $Sc = 1.0$ and for various wave cases: (*a*) S25; (*b*) W25C2; (*c*) W25C14; and (*d*) W25C25.

to the wave surface in these two faster wave cases (figure 3*e–h*). The streamwise velocity variances $\langle u'^2\rangle$ for cases W25C14 (figure 17*g*) and W25C25 (figure 17*h*) show similar wave-correlated distributions as the corresponding $\langle\theta'^2\rangle$.

Consistent with the similarity between the $\langle\theta'^2\rangle$ and $\langle u'^2\rangle$ distributions, the horizontal scalar flux $\langle\theta'u'\rangle$ shown in figure 18 exhibits a similar wave-correlated distribution and wave condition dependence as in $\langle\theta'^2\rangle$ (cf. figure 17). Moreover, the wave-induced variations of $\langle\theta'^2\rangle$ and $\langle\theta'u'\rangle$ are mainly within the viscous wall region $\overline{z}^+ < 50$ (corresponding to $(z-\eta)/\lambda < 0.12$), consistent with the wave-affected region of the time- and plane-averaged profiles $\overline{\theta'}^+_{rms}$ and $\overline{\theta'u'}^+$ shown in figure 15.

Figure 19 shows the contours of the vertical scalar flux $\langle-\theta'w'\rangle$. Similar to $\langle\theta'^2\rangle$ and $\langle u'^2\rangle$, the presence of surface waves also induces significant wave-correlated variation in $\langle-\theta'w'\rangle$. In cases S25 and W25C2, the maximum $\langle-\theta'w'\rangle$ is located above the trough, in a region close to the region of maximum $\langle u'^2\rangle$ (cf. figure 17*e*,*f*). In cases W25C14 and W25C25, the maximum $\langle-\theta'w'\rangle$ is located above the leeward face of the crest. Moreover, there exists a distinct negative $\langle-\theta'w'\rangle$ region above the windward face of the crest, which does not exist in flat-wall boundary layer turbulence. The negative $\langle-\theta'w'\rangle$ region is insignificant in cases S25 and W25C2, but is prominent in cases W25C14 and W25C25. The distinct wave-induced negative $\langle-\theta'w'\rangle$ region near the windward face causes the time and plane average of $\overline{-\theta'w'}^+$ in the viscous sublayer to be significantly lower than that above a flat surface, as shown in figures 15(*f*) and 16(*f*).

A similar distinct negative vertical flux region was found for the Reynolds stress $\langle-u'w'\rangle$ in turbulence over intermediate and fast waves in the DNS studies by Yang & Shen (2009, 2010). Recently, the existence of the negative $\langle-u'w'\rangle$ region has also been observed in the laboratory experiment of Buckley & Veron (2016) using the particle image velocimetry technique. Yang & Shen (2009) studied the characteristics of coherent vortical structures in turbulence over progressive surface waves, and suggested that the significant negative Reynolds stress above the windward face is caused by the vertically bent quasi-streamwise vorticies. A similar mechanism is expected for generating the negative $\langle-\theta'w'\rangle$, which is studied in more detail in § 4.6.

https://doi.org/10.1017/jfm.2017.164 Published online by Cambridge University Press

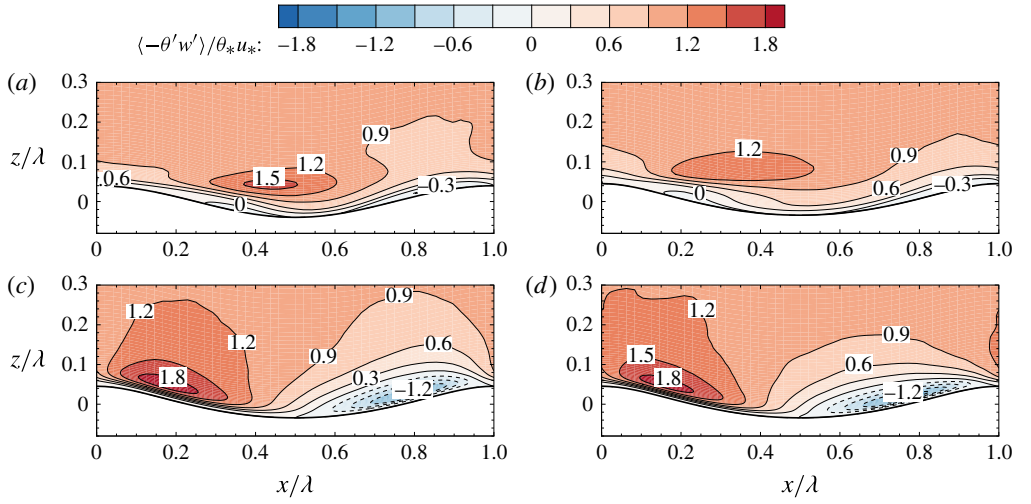


FIGURE 19. (Colour online) Contours of $\langle -\theta' w' \rangle / \theta_* u_*$ for $Sc = 1.0$ and for various wave cases: (*a*) S25; (*b*) W25C2; (*c*) W25C14; and (*d*) W25C25.

4.6. *Correlation between scalar and vortical structures*

Coherent vortical structures in turbulent boundary layer play an important role in the mixing and transport of momentum as well as scalars (e.g. Robinson 1991; Kawamura *et al.* 1998; Zedler & Street 2001; Choi & Suzuki 2005; Wallace 2016). In this subsection, the correlation between vortical structures and scalar fluctuations and fluxes is studied by direct observation of instantaneous vortices and the scalar field, and by conditional averages.

Figure 20 shows the instantaneous vortical structures and scalar fluctuations in the slow wave case W25C2. In particular, the vortices are visualized using the λ_2 method (Jeong & Hussain 1995). Based on the DNS data, the strain-rate tensor $\boldsymbol{S}$ and the rotation tensor $\boldsymbol{\Omega}$ are calculated, and λ_2 is the second largest eigenvalue of the tensor $\boldsymbol{S}^2 + \boldsymbol{\Omega}^2$. In the flow field, the regions with $\lambda_2 < 0$ correspond to the interior of vortices (Jeong & Hussain 1995). Moreover, in figure 20(*a*) the instantaneous vortices are coloured based on the streamwise vorticity, i.e. white if $\omega_x > 0$ and black if $\omega_x < 0$. In figure 20(*a*), several characteristic instantaneous vortices can be observed: reversed horseshoe vortices A and B, and quasi-streamwise vortices C–E. In particular, these reversed horseshoe vortices have their heads upstream and the two legs extended downstream, with $\omega_x > 0$ for the left leg and $\omega_x < 0$ for the right leg (observed when facing the $+x$-direction).

The correlation between these characteristic vortices and the scalar fluctuations can be clearly seen in figure 20(*b*,*c*). The reversed horseshoe vortices A and B are located above the wave trough. Taking vortex B as an example, the rotating motions of its head and two legs induce strong sweep motion ($w' < 0$) towards the wave trough and bring high θ downwards, resulting in $\theta' > 0$ and $-\theta' w' > 0$ (figure 20*b*). The effect of the reversed horseshoe vortex A on the scalar transport is similar to that of vortex B. Vortices C and D appear as a counter-rotating pair, and induce an upwelling motion (i.e. $w' > 0$) between them. Because on average θ increases with height, the upwelling flow ejects low θ upwards and generates a region of $\theta' < 0$; the combination of $w' > 0$ and $\theta' < 0$ results in a region with $-\theta' w' > 0$ between vortices C and D (figure 20*c*).

https://doi.org/10.1017/jfm.2017.164 Published online by Cambridge University Press

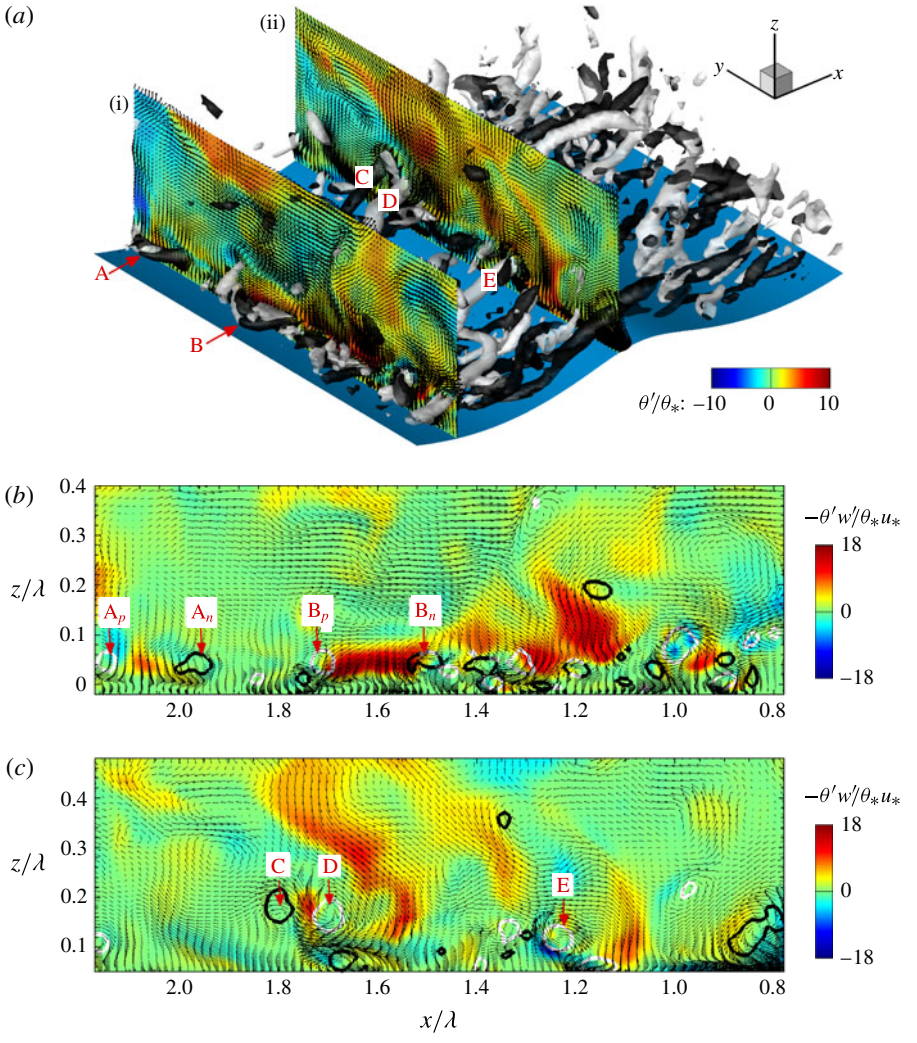


FIGURE 20. (Colour online) Instantaneous flow and scalar fields in turbulence over the slow wave (case W25C2, $Sc = 1.0$). Here only a small portion of the simulation domain is shown for illustration purposes. In (*a*), five characteristic vortices are marked, i.e. the reversed horseshoe vortices A and B and the quasi-streamwise vortices C–E. Two (y, z)-planes at the leeward face (plane i) and crest (plane ii) are plotted, with the contours of θ'/θ_* and vectors of (v', w') shown simultaneously. Zoom-in views of planes (i) and (ii) are plotted with the contours of $-\theta' w'/\theta_* u_*$ shown in (*b*) and (*c*), respectively. The instantaneous vortices are identified by the iso-surface of $\lambda_2 = -0.02$, with white colour for $\omega_x > 0$ and black colour for $\omega_x < 0$. In (*b*), the leg of vortex A with $\omega_x > 0$ is labelled as A_p, and the one with $\omega_x < 0$ is labelled as A_n. Similar notations are used to mark the two legs of vortex B.

The single quasi-streamwise vortex E generates a downwelling event ($w' < 0$) on its right side that brings high θ downwards and results in $\theta' > 0$ and $-\theta' w' > 0$ there.

The above correlations between the vortices and scalar fluctuations in the slow wave case are similar to those in turbulence over flat boundaries (see the reviews

https://doi.org/10.1017/jfm.2017.164 Published online by Cambridge University Press

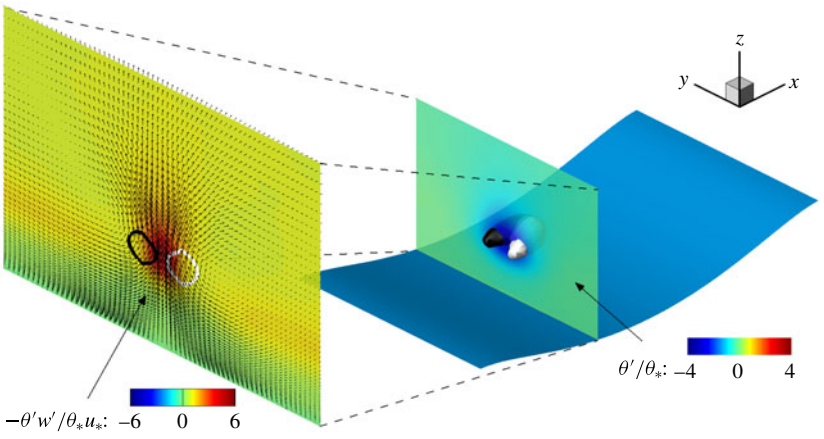


FIGURE 21. (Colour online) Educed flow and scalar fields for case W25C2 with $Sc = 1.0$ by conditional average of the Q2 events above the wave trough. The horseshoe vortex is visualized by the iso-surfaces of $\lambda_2 = -0.002$, with white colour on the leg with $\omega_x > 0$ and black colour on the leg with $\omega_x < 0$. Contours of θ'/θ_* are shown on the vertical plane across the two legs. Contours of $-\theta'w'/\theta_*u_*$ and vectors of (v', w') are shown in the zoom-in view of the vertical plane, on which the thick white and black lines are the iso-contour lines of $\lambda_2 = -0.002$.

by Robinson 1991; Wallace 2016). As shown by the statistical analysis in Yang & Shen (2009, 2010), in turbulence over progressive surface waves, different types of characteristic vortices are present for different wave conditions, and these different characteristic vortices also have different preferential locations relative to the surface waves. In the case of slow waves, reversed horseshoe vortices are usually generated above the wave trough, and then break up into quasi-streamwise vortices as their legs are stretched downstream (Yang & Shen 2009). Then the quasi-streamwise vortices are convected downstream and lifted upwards over the succeeding wave crests and troughs. The combination of the wave-phase-dependent distribution of the coherent vortices and their strong correlations with the scalar fluctuations provides a mechanism for generating the wave-correlated distributions of the scalar variance $\langle\theta'^2\rangle$ (figure 17) and the scalar fluxes $\langle\theta'u'\rangle$ (figure 18) and $\langle-\theta'w'\rangle$ (figure 19).

The correlation between vortices and scalar fluctuations can be further investigated by a conditional average based on the quadrants of the vertical turbulent flux (Wallace 2016). Similar to the quadrant analysis for Reynolds stress, the vertical scalar flux $\langle-\theta'w'\rangle$ can be divided into four quadrants based on the signs of θ' and w': Q1 ($\theta' > 0$, $w' > 0$), Q2 ($\theta' < 0$, $w' > 0$), Q3 ($\theta' < 0$, $w' < 0$) and Q4 ($\theta' > 0$, $w' < 0$). The coherent flow structure related to a specific quadrant can be educed by conditionally sampling and averaging the instantaneous flow events of the chosen quadrant. A brief introduction to the quadrant conditional average scheme used in the current analysis is given in appendix C.

For case W25C2, quadrant analysis indicates that the strong vertical scalar flux above the wave trough shown in figure 19(*b*) is mainly due to the Q2 and Q4 events (see figure 30). By applying the quadrant-based conditional average above the wave trough, the coherent flow structures associated with the Q2 and Q4 events can be educed. Figure 21 shows that a horseshoe vortex (with its head on the downstream

https://doi.org/10.1017/jfm.2017.164 Published online by Cambridge University Press

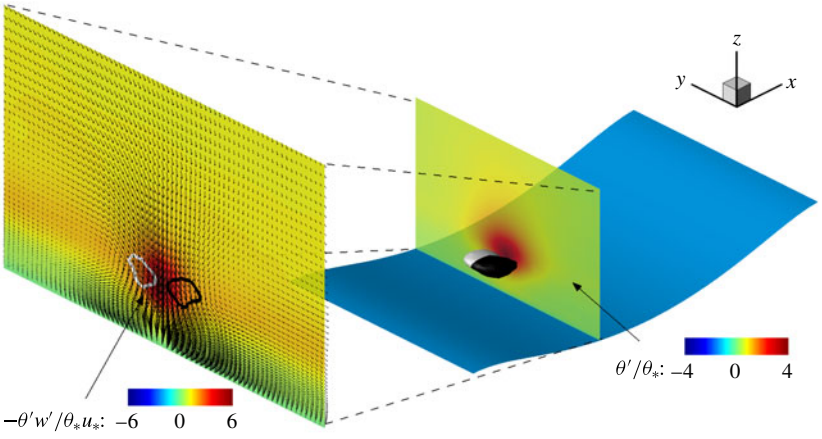


FIGURE 22. (Colour online) Educed flow and scalar fields for case W25C2 with $Sc = 1.0$ by conditional average of the Q4 events above the wave trough. The reversed horseshoe vortex is visualized by the iso-surface of $\lambda_2 = -0.0008$, with white colour on the leg with $\omega_x > 0$ and black colour on the leg with $\omega_x < 0$. Contours of θ'/θ_* are shown on the vertical plane across the two legs. Contours of $-\theta'w'/\theta_*u_*$ and vectors of (v', w') are shown in the zoom-in view of the vertical plane, on which the thick white and black lines are the iso-contour lines of $\lambda_2 = -0.0008$.

side) is educed by a conditional average of Q2 events above the wave trough. Such a vortex induces ejection of lower θ upwards (since θ has lower value near the bottom boundary), which results in $\theta' < 0$ and $-\theta'w' > 0$ between the two legs. It should be pointed out that direct observation of the instantaneous snapshots suggests the presence of quasi-streamwise vortices and horseshoe vortices (with the heads located downstream relative to the legs) in this flow region, both of which contribute to the Q2 events. Because the quadrant-based conditional average does not distinguish these two types of vortices, the educed flow field in figure 21 should account for the contribution of both types of vortices.

Figure 22 shows the conditionally averaged flow and scalar fields for Q4 events in case W25C2. The educed vortical structure exhibits a clear reversed horseshoe shape located slightly above the wave trough, which represents well the instantaneous reversed horseshoe vortices observed from the instantaneous snapshots (figure 20). The reversed horseshoe vortex induces downwelling motion that sweeps high θ towards the wave trough, which results in $\theta' > 0$ and $-\theta'w' > 0$ between the two legs. The reversed horseshoe vortex educed from Q4 events (figure 22) is located lower than the vortex pair educed from Q2 events (figure 21).

Different from the slow wave case discussed above, in the intermediate (W25C14) and fast (W25C25) wave cases the dominant flow structures are the vertically bent quasi-streamwise vortices, e.g. the vortices A–D shown in figure 23(*a*). Yang & Shen (2009) showed that the characteristics of coherent vortices in turbulence over intermediate and fast waves are very similar, with the difference mainly in the population and intensity of the vortices. Therefore, the analysis here focuses on the intermediate wave case W25C14 as a representative case. Figure 23 shows the instantaneous vortex and scalar fields in case W25C14, and figure 24 shows a sketch that illustrates the correlation between a vortex and the vertical scalar flux. In a

https://doi.org/10.1017/jfm.2017.164 Published online by Cambridge University Press

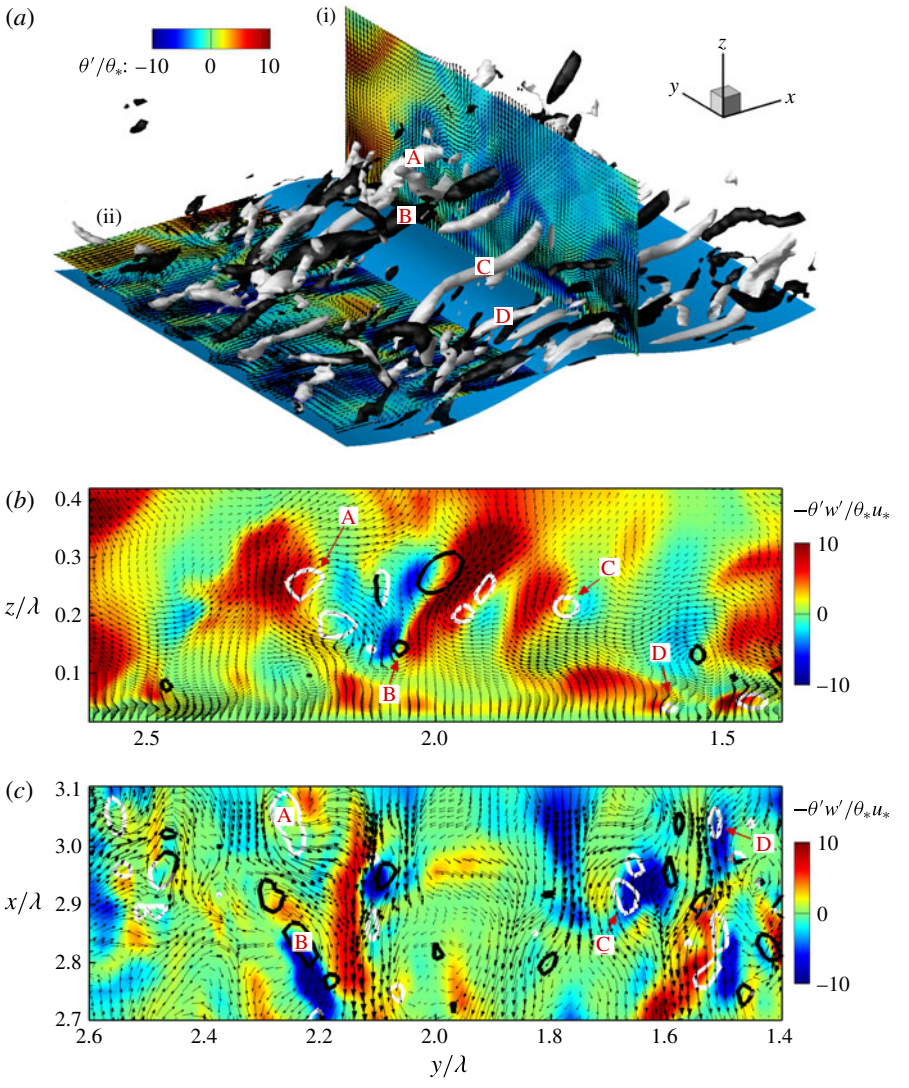


FIGURE 23. (Colour online) Instantaneous flow and scalar fields in turbulence over the intermediate wave (case W25C14, $Sc = 1.0$). Only a small portion of the simulation domain is shown for illustration purposes. Four characteristic vertically bent quasi-streamwise vortices (A–D) are marked. In (*a*), the instantaneous vortices are identified by the iso-surface of $\lambda_2 = -0.02$, with white colour for $\omega_x > 0$ and black colour for $\omega_x < 0$. The (y, z)-plane above the leeward face (plane i) and the (x, z)-plane above the windward face (plane ii) are plotted, with the contours of θ'/θ_* and vectors of velocity fluctuation (the components parallel to each plane) shown simultaneously. Panels (*b*) and (*c*) show the contours of the scalar flux $-\theta' w'/\theta_* u_*$ on planes (i) and (ii), respectively. In (*b*) and (*c*), the locations of the vortices are indicated by the iso-contours of $\lambda_2 = -0.02$, with white colour for $\omega_x > 0$ and black colour for $\omega_x < 0$.

reference frame moving at the wave phase speed, the near-surface vortices travel backwards in the $-x$-direction (see the mean streamlines shown in figure 3). They appear to be straight and horizontally oriented above the leeward face and the crest,

https://doi.org/10.1017/jfm.2017.164 Published online by Cambridge University Press

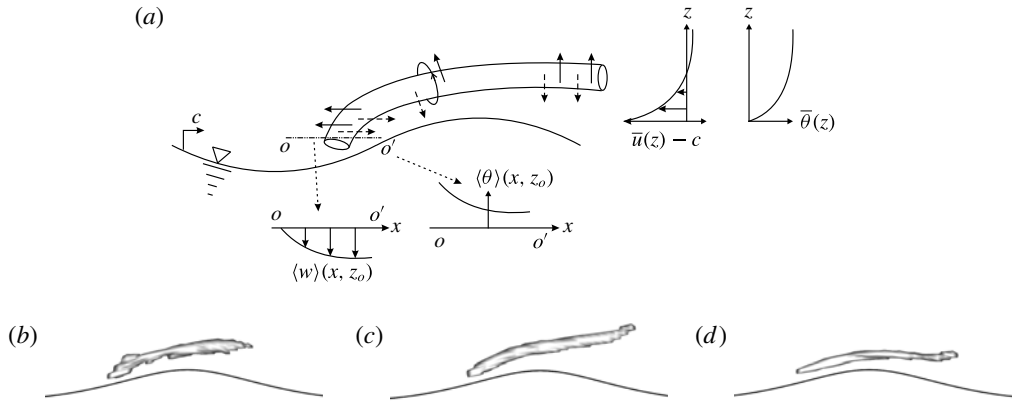


FIGURE 24. Sketch of the characteristic vortical structure (i.e. the vertically bent quasi-streamwise vortex) in turbulence over intermediate and fast waves. Panel (*a*) illustrates the correlation between the vortex and the turbulent fluctuations of velocity and scalar. The arrows near the vortex indicate the velocity fluctuation vectors associated with the vortex, with solid arrows in front of the vortex and dashed arrows behind the vortex. Panels (*b–d*) show three representative samples of the instantaneous vortices extracted from the DNS data of case W25C14.

and then bend downwards as they travel over the windward face. The unique shape and wave-phase correlation of the vortices result in the wave-correlated scalar flux shown in figure 19(*c*,*d*).

Taking the vortex C in figure 23 as an example, its horizontal part above the leeward face induces an upwelling motion (i.e. $w' > 0$) on its left side (observed when facing the $+x$-direction), which ejects low θ upwards and results in $\theta' < 0$ (see plane-i in figure 23*a*) and leads to a Q2 flux $-\theta' w' > 0$ (figure 23*b*). This mechanisms is similar to the Q2 flux generation mechanism in case W25C2. On the other hand, the vertical part of the vortex C above the windward face induces a horizontal velocity fluctuation $u' < 0$ on its left side (observed when facing the $+x$-direction), which induces a vertical velocity fluctuation $w' < 0$ because $\partial\langle w\rangle/\partial x < 0$ there (Yang & Shen 2009) (also see figure 3*e* and the sketch in figure 24*a*). Similarly, the fluctuation $u' < 0$ induces a scalar fluctuation of $\theta' < 0$ because $\partial\langle\theta\rangle/\partial x < 0$ there (figure 3*f* and the sketch in figure 24*a*). These correlations result in $\theta' u' > 0$ and $-\theta' w' < 0$ above the windward face of the wave crest, as shown in figures 18(*c*) and 19(*c*), respectively.

Similar to case W25C2, a quadrant-based conditional average can be done for case W25C14 to educe a statistical description of the correlation between vortical structures and scalar fluxes. As shown in figure 31 in the appendix C, in case W25C14 the positive vertical scalar flux $-\theta' w'$ above the leeward face is mainly due to the Q2 and Q4 events, while the negative vertical scalar flux above the windward face is mainly due to the Q1 and Q3 events. This result is consistent with the direct observation of the instantaneous flow and scalar fields shown in figure 23. Based on these wave-phase preferences, Q2 and Q4 events are conditionally sampled above the leeward face, and Q1 and Q3 events are conditionally sampled above the windward face. The specific locations where quadrant events detectors are applied are marked in figure 31.

Figure 25 shows the conditionally averaged Q2 event above the leeward face of case W25C14. Note that unlike in figures 21 and 22 where the vortices are visualized by

https://doi.org/10.1017/jfm.2017.164 Published online by Cambridge University Press

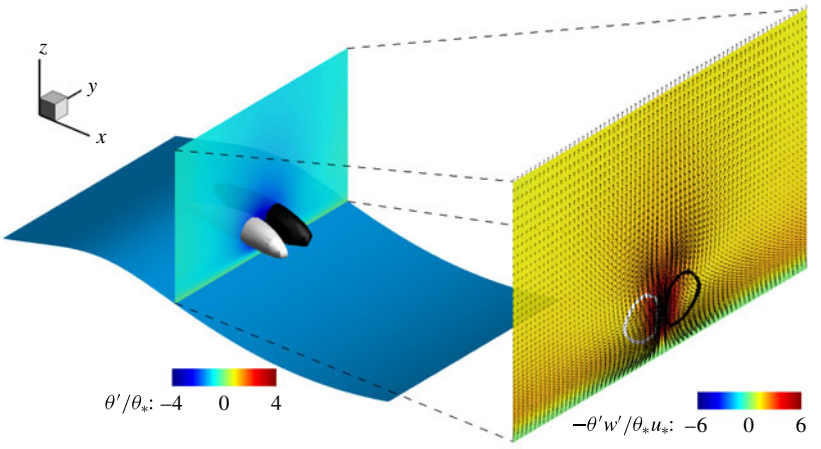


FIGURE 25. (Colour online) Educed flow and scalar fields for case W25C14 with $Sc = 1.0$ by conditional average of the Q2 events above the leeward face of the wave crest. The pair of vortices are visualized by the iso-surfaces of $|\omega_x/(u_*^2/\nu)| = 0.05$, with white colour for $\omega_x > 0$ and black colour $\omega_x < 0$. Contours of θ'/θ_* are shown on the vertical plane across the vortex pair. Contours of $-\theta' w'/\theta_* u_*$ and vectors of (v', w') are shown in the zoom-in view of the vertical plane, on which the thick white and black lines are the iso-contour lines of $\omega_x/(u_*^2/\nu) = 0.05$ and -0.05, respectively.

the λ_2 method, in figure 25 the vortices are visualized using the iso-surfaces of $|\omega_x|$. This is because in turbulence over intermediate and fast propagating surface waves (as well as in oscillating flow over stationary waves), the strong relative oscillation between the mean flow and the surface waves generates thin vortex sheets with significant spanwise vorticity in the vicinity of the wave crests and troughs (e.g. Tseng & Ferziger 2003; Yang & Balaras 2006; Yang & Shen 2009). In figure 23, those thin vortex sheets have been removed to provide a clear visualization of other coherent flow structures. However, because of their persistent presences at fixed wave phases (i.e. above crests and troughs), these vortex sheets also appear in the conditionally averaged field, with magnitudes larger than those of the vortices associated with the quadrant events. As a result, the desired vortices would not be clearly seen when the λ_2 method is used for visualization. Instead, the iso-surfaces of $|\omega_x|$ are good alternative for visualization because the horizontal part of a quasi-streamwise vortex above the leeward face in case W25C14 has a significant streamwise vorticity ω_x. Similarly, the iso-surfaces of $|\omega_z|$ are used for visualizing the vertical part of the vortex above the windward face. As shown in figure 25, the conditional average of Q2 events exhibits a pair of counter-rotating streamwise vortices above the leeward face, which induce upwelling motion ($w' > 0$) between them and result in $\theta' < 0$ and $-\theta' w' > 0$. Note that in figure 25 the vortices appear in pairs because the Q2 events generated by vortices with $\omega_x > 0$ and $\omega_x < 0$ are both sampled and included in the averaging process. In the instantaneous snapshots, these vortices usually appear individually.

A similar quadrant-based conditional average can be applied for all the four quadrants. Figure 26 shows the results for the four quadrants. Note that, as discussed above, in figure 26(*a*,*c*) the vortices are visualized using the iso-surfaces of $|\omega_z|$, while in figure 26(*b*,*d*) the vortices are visualized based on $|\omega_x|$. For all the four quadrants

https://doi.org/10.1017/jfm.2017.164 Published online by Cambridge University Press

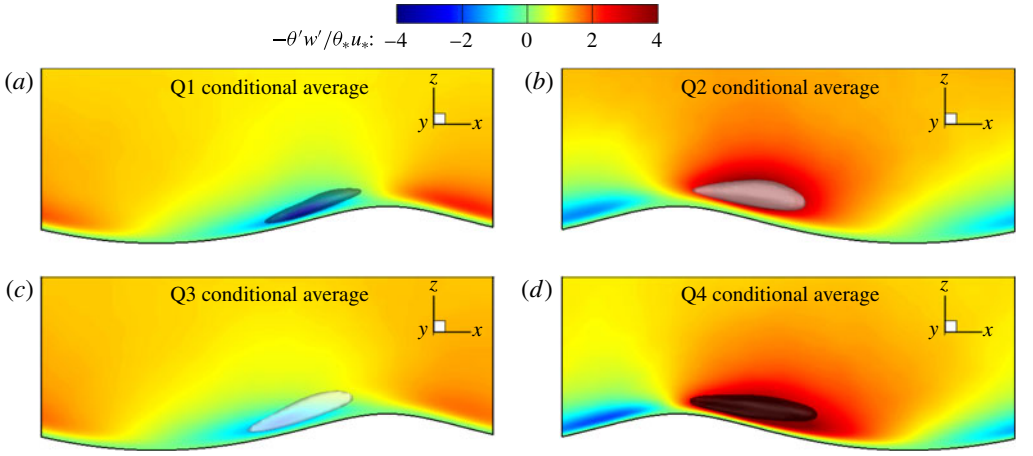


FIGURE 26. (Colour online) Side view of the educed flow and scalar fields for case W25C14 with $Sc = 1.0$ by conditional average based on the four different quadrants of $\langle -\theta'w' \rangle$: (*a*) Q1 ($\theta' > 0, w' > 0$) events above the windward face; (*b*) Q2 ($\theta' < 0, w' > 0$) events above the leeward face; (*c*) Q3 ($\theta' < 0, w' < 0$) events above the windward face; and (*d*) Q4 ($\theta' > 0, w' < 0$) events above the leeward face. In the figure, the colour contours are for $-\theta'w'/\theta_*u_*$ on the (x, z)-plane across the centre of the educed field. In each panel, the vortical structures are represented by the iso-surfaces of (*a*) $\omega_z/(u_*^2/\nu) = -0.05$, (*b*) $\omega_x/(u_*^2/\nu) = 0.05$, (*c*) $\omega_z/(u_*^2/\nu) = 0.05$, and (*d*) $\omega_x/(u_*^2/\nu) = -0.05$, respectively. In particular, light colour iso-surfaces correspond to positive vorticities (i.e. $\omega_x > 0$ or $\omega_z > 0$) and dark colour ones correspond to negative vorticities (i.e. $\omega_x < 0$ or $\omega_z < 0$).

the educed vortices appear in pair, but only the ones in front of the central (x, z)-plane of the averaged field are shown in figure 26. Both the conditionally averaged vortices and the scalar flux fields agree with the observation of the instantaneous snapshot in figure 23 and the phase-averaged scalar flux contours in figures 19(*c*) and 31.

It should be noted that the characteristics of the vortical structures may vary with the Reynolds number. The results presented in § 4.6 are based on DNS with a Reynolds number lower than that in a real marine wind condition. Therefore, caution should be taken when interpreting the vortical structures reported in this DNS study and linking them to those in the more realistic field condition. Nevertheless, the vortical structures found in the current DNS as well as their correlations with the distribution of scalar flux still provide useful insights for explaining the flow structures over progressive waves on a laboratory scale such as the recent experiment by Buckley & Veron (2016), in which they observed negative Reynolds stress above the windward face of air flow over fast propagating surface waves similar to the results obtained from the current DNS (see figures 19, 26 and 31).

5. Conclusions

Scalar transport in air turbulence over progressive surface waves plays an important role in air–sea interaction. The presence of progressive waves at the sea surface imposes great challenges to modelling the turbulent flow and scalar transport above the waves. To tackle this complex problem, in this study a wave boundary-fitted DNS turbulence solver previously developed by Yang & Shen (2011*a*) is employed, and is further expanded by including a scalar transport solver also based on the

https://doi.org/10.1017/jfm.2017.164 Published online by Cambridge University Press

boundary-fitted computational grid system. This expanded DNS model is shown to be able to capture the details of the complex scalar transport phenomena in the vicinity of the wave surface.

Using the DNS, the effects of surface wave motions on the scalar transport are studied in detail. In particular, three representative wave ages (i.e. the wave phase speed normalized by the wind friction velocity) are considered, representing the slow, intermediate and fast wave conditions, respectively. Statistical analyses of the DNS data show a strong wave phase dependence in the distributions of scalar concentration, scalar variance, turbulent scalar fluxes, and local Sherwood number along the wave surface. Comparison of the statistics among different wave conditions also reveals a significant effect of the wave age on the scalar transport.

The wave age effect is also pronounced in the time and plane average of these quantities, suggesting the importance of including the surface wave effect in models that cannot directly capture the wave-phase-induced disturbance. In particular, the vertical profiles of the time- and plane-averaged scalar for various wave conditions exhibit similar structures to those found in turbulence over a flat wall, i.e. a linear profile in the near-surface viscous sublayer ($\overline{z}^+ < 5$ in wall unit) and a logarithmic profile in the displaced log-law region ($50 < \overline{z}^+ < 150$). However, the von Kármán constant and the effective wave surface roughness for the mean scalar profile exhibit considerable variation with the wave age. The effect of the Schmidt number on the time and plane average of scalar is also quantified, which is found to be similar to that in flat-wall turbulence.

Moreover, the profiles of the root-mean-square scalar fluctuation and the horizontal scalar flux exhibit good scaling behaviours in the viscous sublayer that agree with the scaling laws previously reported for flat-wall turbulence, but considerable wave-induced variation is found in the viscous wall region above the sublayer ($5 < \overline{z}^+ < 50$). In addition, the profiles of the vertical scalar flux in the viscous sublayer over surface waves exhibit considerable discrepancies from the reported scaling law for the flat-wall turbulence. A close look at the two-dimensional contours of the phase-averaged vertical scalar flux indicates that the discrepancy is caused by a negative vertical flux region above the windward face of the wave crest, especially in the intermediate and fast wave cases.

Detailed analyses show that the instantaneous scalar fluctuations and fluxes are highly correlated with the coherent vortical structures in the turbulence above the wave surface, which exhibit clear wave-dependent characteristics in terms of their shapes and preferential locations. In particular, the characteristic vortices vary from quasi-streamwise (above windward face) and reversed horseshoe (above trough) shapes in the slow wave case, to vertically bent vortices over wave crests in the intermediate and fast wave cases. Direct observation of the instantaneous snapshots as well as quadrant-based conditional average analysis indicates that the wave age dependence of the wave-correlated scalar variance and flux distributions is caused by the combined effects of the characteristic vortices, their preferential locations, and the local gradient of the scalar concentration in the vicinity of these vortices.

It should be noted that in real open-sea conditions, the wind-generated waves usually have a broadband spectrum, with short waves steeper and propagating slower than long waves. Certain wave modes may also have an oblique angle relative to main wind direction. These effects are not considered in the current DNS study with a canonical configuration, and should be investigated in future studies.

https://doi.org/10.1017/jfm.2017.164 Published online by Cambridge University Press

Acknowledgements

D.Y. acknowledges financial support from his start-up funds as well as technical support from the Center for Advanced Computing and Data Systems (CACDS) and the Research Computing Center (RCC) at the University of Houston to carry out the simulations presented here. The support to L.S. through the ONR CASPER MURI project (N00014-16-1-3205) and the NSF award OCE-1341063 is gratefully acknowledged.

Appendix A. Validation with flat-wall case

To validate the DNS flow and scalar solvers, a series of test cases for turbulent Couette flows with a flat bottom boundary are performed. In particular, three different Reynolds numbers $Re_* = u_*\delta/\nu = 180$, 283, and 455 are considered, where δ is the half domain height. For each Reynolds number, four different Schmidt numbers, $Sc = 0.4$, 0.71, 1.0, and 3.0, are considered. These DNS results are compared with experimental and numerical results collected from the literature.

Figure 27 shows the profiles of mean streamwise velocity $\overline{u}^+$ and velocity fluctuation r.m.s. ($\overline{u'}^+_{rms}$, $\overline{v'}^+_{rms}$, $\overline{w'}^+_{rms}$). The current DNS results agree well with the experimental and DNS results in the literature for turbulent Couette flows and channel flows. In figure 27(*a*), the mean velocity profile obeys a linear law of $\overline{u}^+ = z^+$ in the viscous sublayer at $z^+ < 5$, and a logarithmic law of $\overline{u}^+ = (1/0.41)\ln(z^+) + 5.2$ in the log-law region at $z^+ > 30$. In figure 27(*b*), the velocity fluctuation r.m.s. exhibits anisotropy, with the magnitude of $\overline{u'}^+_{rms}$ larger than the other two components. Note that in turbulent Couette flow the vertical gradient of the mean velocity remains finite so that the velocity fluctuations reach a plateau towards the centre of the channel and remain anisotropic, while in a turbulent channel flow the streamwise velocity fluctuation r.m.s. magnitude reduces more significantly towards the centre of the channel (Debusschere & Rutland 2004). Therefore, in figure 27(*b*) only the results for turbulent Couette flows in the literature are plotted.

Figure 28 shows the profiles of mean scalar $\overline{\theta}^+$ and scalar fluctuation r.m.s. $\overline{\theta'}^+_{rms}$. Similar to the mean velocity, the profiles of $\overline{\theta}^+$ also exhibit a linear profile in the viscous sublayer and a logarithmic profile in the log-law region. The DNS results at different Re_* show only very small differences in $\overline{\theta}^+$. The change of Schmidt number has a more significant effect, with $\overline{\theta}^+$ increasing as Sc increases. By compiling a collection of experimental data, Kader (1981) found that the near-wall linear profile of the mean scalar follows

$$\overline{\theta}^+ = Sc\, z^+, \tag{A 1}$$

and the log-law profile follows

$$\overline{\theta}^+ = \frac{1}{\kappa_\theta}\ln(z^+) + B_\theta(Sc), \tag{A 2}$$

where $\kappa_\theta = 0.47$ and

$$B_\theta(Sc) = (3.84Sc^{1/3} - 1.3)^2 + 2.12\ln(Sc). \tag{A 3}$$

As shown in figure 28(*a*), the mean scalar profiles for various Re_* and Sc obtained from the current DNS agree well with the scaling laws given by (A 1)–(A 3) in the corresponding linear and logarithmic regions. Similarly, the profiles of $\overline{\theta'}^+_{rms}$ also agree well with the previous DNS result from Debusschere & Rutland (2004) and the linear scaling law found by Antonia & Kim (1991) and Kawamura *et al.* (1998).

https://doi.org/10.1017/jfm.2017.164 Published online by Cambridge University Press

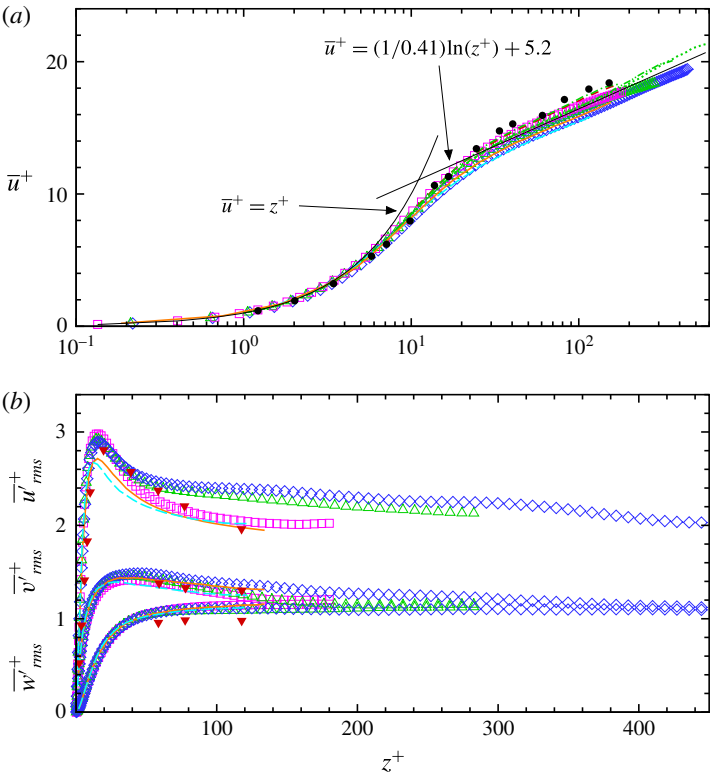


FIGURE 27. (Colour online) Profiles of (*a*) mean streamwise velocity $\overline{u}^+$ and (*b*) velocity fluctuation r.m.s. ($\overline{u'^+_{rms}}$, $\overline{v'^+_{rms}}$, $\overline{w'^+_{rms}}$) in turbulent flows over a flat boundary. Experimental data are denoted by solid symbols: ●, channel flow at $Re_* = 142$ from Eckelmann (1974) (modified by Kim *et al.* 1987); +, Couette flow at $Re_* = 82$ from Aydin & Leutheusser (1991); ×, Couette flow at $Re_* = 134$ from Aydin & Leutheusser (1991); ▼, Couette flow at $Re_* = 434$ from El Telbany & Reynolds (1982). DNS results are denoted by lines: – – –, channel flow at $Re_* = 180$ from Kim *et al.* (1987); — · —, channel flow at $Re_* = 180$ from Moser, Kim & Mansour (1999); — · · —, channel flow at $Re_* = 395$ from Moser *et al.* (1999); · · · , channel flow at $Re_* = 590$ from Moser *et al.* (1999); – –, Couette flow at $Re_* = 120$ from Sullivan *et al.* (2000); ——, Couette flow at $Re_* = 157$ from Papavassiliou & Hanratty (1997). The current DNS results of Couette flows are denoted by open symbols: □, $Re_* = 180$; △, $Re_* = 283$; ◇, $Re_* = 445$. In (*a*), the reference linear profile $\overline{u}^+ = z^+$ and logarithmic profile $\overline{u}^+ = (1/0.41)\ln(z^+) + 5.2$ are denoted by thin solid lines.

Appendix B. Averaging on ζ-plane versus on z-plane

In the triple decomposition approach used for analyzing the DNS results (see equation (4.1)), the mean velocity and scalar are calculated by averaging on the planes of constant ζ, which is defined by the grid algebraic mapping equation (2.12). As shown in figure 29(*a*), the grid lines of constant ζ are nearly parallel to the wave surface near the lower boundary of the simulation domain. Thus, computing the mean quantities along ζ-planes allows us to obtain the correct linear profiles in the thin viscous sublayer, which is within 5 wall units above the curved wave surface. Such a thin viscous sublayer cannot be captured if the average is done along z-planes, as

https://doi.org/10.1017/jfm.2017.164 Published online by Cambridge University Press

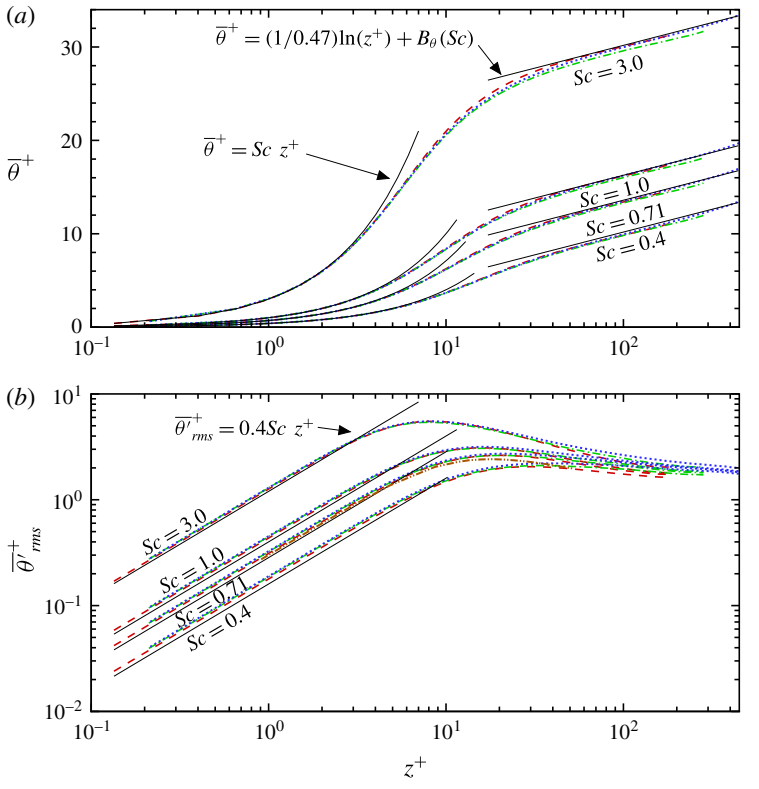


FIGURE 28. (Colour online) Profiles of (*a*) mean scalar $\overline{\theta}^+$ and (*b*) scalar fluctuation r.m.s. $\overline{\theta'}^+_{rms}$ in turbulent flows over a flat boundary. The DNS results for three different Reynolds numbers are shown: – – –, $Re_* = 180$; — · —, $Re_* = 283$; and · · · , $Re_* = 445$. For each Reynolds number, four different Schmidt numbers are shown, i.e. $Sc = 0.4$, 0.71, 1.0 and 3.0. In (*a*), the reference linear profile $\overline{\theta}^+ = Sc\, z^+$ and logarithmic profile $\overline{\theta}^+ = (1/\kappa_\theta)\ln(z^+) + B_\theta(Sc)$ suggested by Kader (1981) are denoted by thin solid lines for each Schmidt number, where $\kappa_\theta = 0.47$ and $B_\theta(Sc) = (3.84Sc^{1/3} - 1.3)^2 + 2.12\ln(Sc)$. In (*b*), the linear reference profile $\overline{\theta'}^+_{rms} = 0.4Sc\, z^+$ for each corresponding Sc is denoted by thin solid lines, and the DNS result from Debusschere & Rutland (2004) for $Re_* = 160$ and $Sc = 0.7$ is denoted by — · · —.

it does not have a valid definition in the flow regions lower than the elevation of the wave crest as shown in figure 29(*b*).

Overall, the mean profiles based on ζ-plane averaging merge to the corresponding mean profiles based on z-plane averaging because the ζ-plane becomes flatter towards higher elevation (see the grid lines in figure 29*a*). Near the wave surface, z-plane averaging yields lower values than the ζ-plane averaging due to the wave-induced distortion. We remark that for a flat-wall turbulent boundary layer, the log-law region is typically defined to be within $30 < z^+ < 0.3\delta^+$, where δ^+ is the half-domain height in wall units (see table 7.1 in Pope 2000). Note that the wave crest in the current study has a height of $\eta^+_{crest} = 17.7$ and the averaged half-domain height is $\delta^+ = 445$, therefore the log-law region in the current DNS should be defined as $50 < z^+ < 150$ considering the additional vertical displacement of the mean profile by the wave crest.

https://doi.org/10.1017/jfm.2017.164 Published online by Cambridge University Press

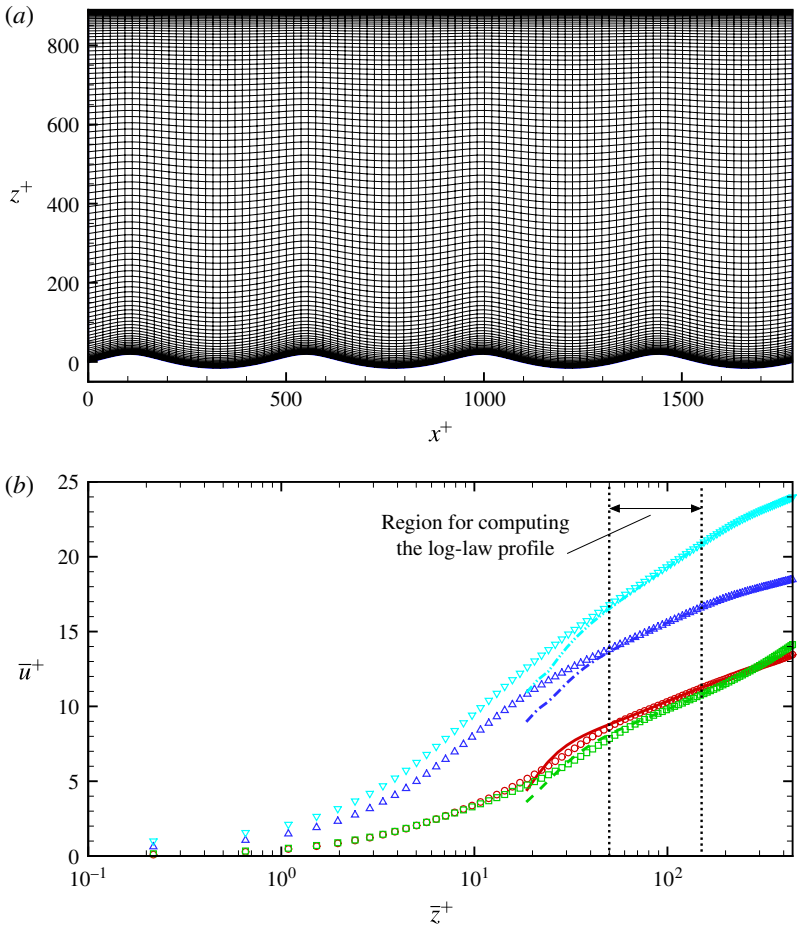


FIGURE 29. (Colour online) Comparison of ζ-plane averaging with z-plane averaging. Panel (a) shows the boundary-fitted computational grid used in the current DNS, with each of the horizontal grid lines corresponding to a constant ζ in the computational space (ξ, ψ, ζ, τ). For illustration purposes, the grid lines on a (x, z)-plane are plotted for every two actual grids used in the simulation. Panel (b) shows the comparison of the mean streamwise velocity $\overline{u}^+$ obtained by averaging on planes of constant ζ (open symbols) versus on planes of constant z (lines): ○ and ——, S25 $(c/u_* = 0)$; □ and − − −, W25C2 $(c/u_* = 2)$; △ and — · —, W25C14 $(c/u_* = 14)$; ▽ and — · · —, W25C25 $(c/u_* = 25)$. When evaluating the log-law profile, the mean velocity within $50 < z^+ < 150$ is used, as marked by the two dotted lines.

Figure 29(b) shows that the mean profiles obtained by ζ-plane averaging and z-plane averaging agree very well in the log-law region. The above analyses show that it is an appropriate choice to compute the mean quantities based on the ζ-plane averaging for the statistical analyses performed in this study.

Appendix C. Conditional average based on quadrants of scalar flux

The vertical turbulent flux of the scalar, $\langle -\theta' w' \rangle$, can be decomposed into four parts based on the quadrants in the (θ', w') space: Q1 $(\theta' > 0, w' > 0)$, Q2 $(\theta' < 0, w' > 0)$,

https://doi.org/10.1017/jfm.2017.164 Published online by Cambridge University Press

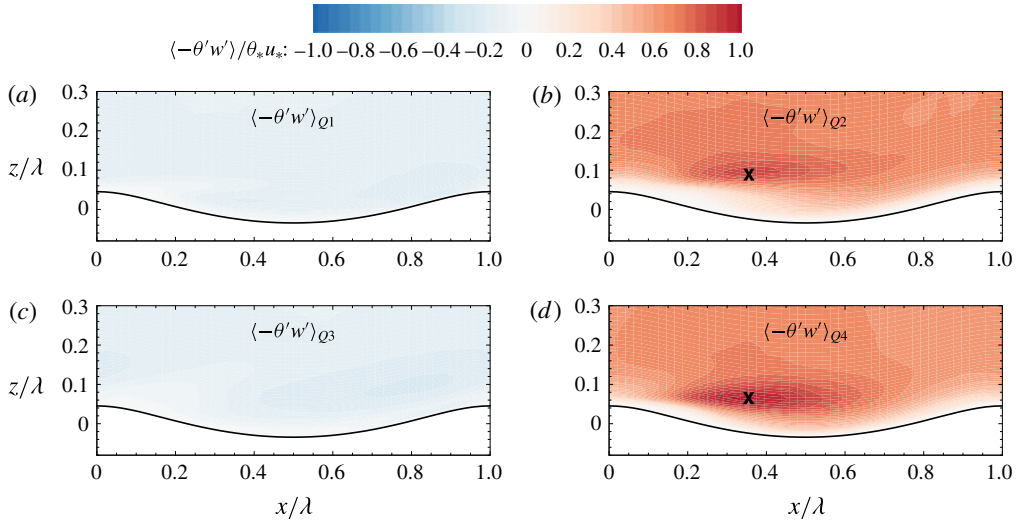


FIGURE 30. (Colour online) Decomposed vertical scalar flux $\langle -\theta' w' \rangle$ for case W25C2 with $Sc = 1.0$ based on the four quadrants: (*a*) Q1 ($\theta' > 0, w' > 0$); (*b*) Q2 ($\theta' < 0, w' > 0$); (*c*) Q3 ($\theta' < 0, w' < 0$); and (*d*) Q4 ($\theta' > 0, w' < 0$). In (*b*) and (*d*), each of the corresponding detection position for quadrant-based conditional sampling is chosen to be the grid point at the maximum of the corresponding quadrant and is marked by the cross symbol. In case W25C2, the Q1 and Q3 events contribute very little to $\langle -\theta' w' \rangle$, thus are not considered in the quadrant-based conditional sampling analysis.

Q3 ($\theta' < 0, w' < 0$) and Q4 ($\theta' > 0, w' < 0$). Figures 30 and 31 show the decomposed turbulent scalar flux $\langle -\theta' w' \rangle$ for cases W25C2 and W25C14, respectively. In case W25C2, quadrants Q2 and Q4 make the greatest contributions to the total flux, while the contributions from Q1 and Q3 are significantly smaller. In case W25C14, the four quadrants make comparable contributions to the total flux, with Q1 and Q3 for the negative flux region above the windward face and Q2 and Q4 for the positive flux region above the leeward face. The results for case W25C25 are very similar to those in case W25C14, and are thus not shown here due to space limitations.

For the quadrant-based conditional average shown in § 4.6, samples are taken from the instantaneous snapshots of the velocity and scalar fields using the quadrant events detector (Kim & Moin 1986; Yang & Shen 2009),

$$D_i(y, t; x_s, z_s) = \begin{cases} 1, & \text{if } (\theta', w') \in \mathrm{Q}i \text{ and } \dfrac{-\theta' w'}{\langle -\theta' w' \rangle} > 2, \\ 0, & \text{otherwise.} \end{cases} \tag{C 1}$$

This detection function is applied to a number of instantaneous snapshots at different time t. Samples for quadrant Qi are taken if $D_i(y, t; x_s, z_s) = 1$. Moreover, the detection function scans over all the y for each snapshot, but uses fixed values for (x_s, z_s) for each quadrant event so that samples are taken at a consistent location relative to the wave phase. The (x_s, z_s) location for each quadrant is chosen to be the grid point that has the maximum of the contribution to $\langle -\theta' w' \rangle$ due to the corresponding quadrant, and the specific locations for cases W25C2 and W25C14 are marked in figures 30 and 31, respectively. For each case, 400 instantaneous snapshots of the

https://doi.org/10.1017/jfm.2017.164 Published online by Cambridge University Press

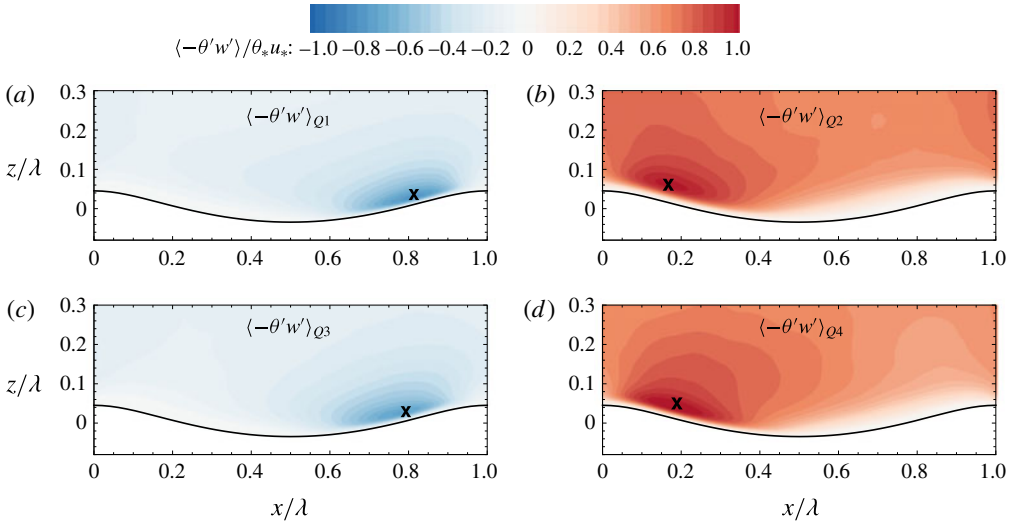


FIGURE 31. (Colour online) Decomposed vertical scalar flux $\langle -\theta' w' \rangle$ for case W25C14 with $Sc = 1.0$ based on the four quadrants: (*a*) Q1 ($\theta' > 0, w' > 0$); (*b*) Q2 ($\theta' < 0, w' > 0$); (*c*) Q3 ($\theta' < 0, w' < 0$); and (*d*) Q4 ($\theta' > 0, w' < 0$). In each panel, the corresponding detection position for quadrant-based conditional sampling is chosen to be the grid point at the maximum of the corresponding quadrant and is marked by the cross symbol.

full three-dimensional velocity and scalar fields are used for conditional average, with each snapshot consisting of four wavelengths. For the analysis reported in this paper, in (C 1) the samples are high-pass filtered by the criterion $-\theta' w' / \langle -\theta' w' \rangle > 2$, i.e. samples are taken only when the magnitude of the detected instantaneous vertical flux is at least twice of the phase-averaged flux at the detection location. In addition to the threshold of 2, other values have also been tested for the high-pass filter criterion (e.g. 0.5, 1, 4 and 8), but insignificant differences were found in the educed flow and scalar fields, suggesting that the conditional average criterion used in the present analysis is representative.

REFERENCES

ANDERSON, D. A., TANNEHILL, J. C. & PLETCHER, R. H. 1984 *Computational Fluid Mechanics and Heat Transfer*. McGraw Hill.

ANTONIA, R. A. & KIM, J. 1991 Turbulent Prandtl number in the near-wall region of a turbulent channel flow. *Intl J. Heat Mass Transfer* **34**, 1905–1908.

AYDIN, E. M. & LEUTHEUSSER, H. J. 1991 Plane-Couette flow between smooth and rough walls. *Exp. Fluids* **11**, 302–312.

BANNER, M. L. & MELVILLE, W. K. 1976 On the separation of air flow over water waves. *J. Fluid Mech.* **77**, 825–842.

BELCHER, S. E. & HUNT, J. C. R. 1998 Turbulent flow over hills and waves. *Annu. Rev. Fluid Mech.* **30**, 507–538.

BOURASSA, M. A., VINCENT, D. G. & WOOD, W. L. 1999 A flux parameterization including the effects of capillary waves and sea state. *J. Atmos. Sci.* **56**, 1123–1139.

BUCKLEY, M. P. & VERON, F. 2016 Structure of the airflow above surface waves. *J. Phys. Oceanogr.* **46**, 1377–1397.

CHARNOCK, H. 1955 Wind stress on a water surface. *Q. J. R. Meteorol. Soc.* **81**, 639–640.

https://doi.org/10.1017/jfm.2017.164 Published online by Cambridge University Press

CHOI, H. S. & SUZUKI, K. 2005 Large eddy simulation of turbulent flow and heat transfer in a channel with one wavy wall. *Intl J. Heat Fluid Flow* **26**, 681–694.

CRAFT, T. J. & LAUNDER, B. E. 1996 A Reynolds stress closure designed for complex geometries. *Intl J. Heat Fluid Flow* **17**, 245–254.

DE ANGELIS, V., LOMBARDI, P. & BANERJEE, S. 1997 Direct numerical simulation of turbulent flow over a wavy wall. *Phys. Fluids* **9**, 2429–2442.

DEAN, R. G. & DALRYMPLE, R. A. 1991 *Water Wave Mechanics for Engineers and Scientists*. World Scientific.

DEBUSSCHERE, B. & RUTLAND, C. J. 2004 Turbulent scalar transport mechanisms in plane channel and Couette flows. *Intl. J. Heat Mass Transfer* **47**, 1771–1781.

DECOSMO, J., KATSAROS, K. B., SMITH, S. D., ANDERSON, R. J., OOST, W. A., BUMKE, K. & CHADWICK, H. 1996 Air–sea exchange of water vapor and sensible heat: the humidity exchange of the sea experiment (HEXOS) results. *J. Geophys. Res.* **101** (C5), 12001–12016.

DELLIL, A. Z., AZZI, A. & JUBRAN, B. A. 2004 Turbulent flow and convective heat transfer in a wavy wall channel. *Heat Mass Transfer* **40**, 793–799.

DOMMERMUTH, D. G. & YUE, D. K. P. 1987 A high-order spectral method for the study of nonlinear gravity waves. *J. Fluid Mech.* **184**, 267–288.

DONELAN, M. A. 1990 Air-sea interaction. In *The Sea* (ed. B. LeMehaute & D. M. Hanes), vol. 9, pp. 239–292. Wiley-Interscience.

DONELAN, M. A., BABANIN, A. V., YOUNG, I. R. & BANNER, M. L. 2006 Wave-follower field measurements of the wind-input spectral function. Part II. Parameterization of the wind input. *J. Phys. Oceanogr.* **36**, 1672–1689.

DRUZHININ, O. A., TROITSKAYA, Y. I. & ZILITINKEVICH, S. S. 2012 Direct numerical simulation of a turbulent wind over a wavy water surface. *J. Geophys. Res.* **117**, C00J05.

DRUZHININ, O. A., TROITSKAYAA, Y. I. & ZILITINKEVICH, S. S. 2016 Stably stratified airflow over a waved water surface. Part 1: stationary turbulence regime. *Q. J. R. Meteorol. Soc.* **142**, 759–772.

ECKELMANN, H. 1974 The structure of the viscous sublayer and the adjacent wall region in a turbulent channel flow. *J. Fluid Mech.* **65**, 439–459.

EDSON, J., CRAWFORD, T., CRESCENTI, J., FARRAR, T., FREW, N., GERBI, G., HELMIS, C., HRISTOV, T., KHELIF, D., JESSUP, A. *et al.* 2007 The coupled boundary layers and air-sea transfer experiment in low winds. *Bull. Am. Meteorol. Soc.* **88**, 342–356.

EDSON, J. B., ZAPPA, C. J., WARE, J. A., MCGILLIS, W. R. & HARE, J. E. 2004 Scalar flux profile relationships over the open ocean. *J. Geophys. Res.* **109**, C08S09.

EL TELBANY, M. M. M. & REYNOLDS, A. J. 1982 The structure of turbulent plane Couette. *Trans. ASME J. Fluids Engng* **104**, 367–372.

FAIRALL, C. W., BRADLEY, E. F., ROGERS, D. P., EDSON, J. B. & YOUNG, G. S. 1996 Bulk parameterization of air-sea fluxes for tropical ocean-global atmosphere coupled-ocean atmosphere response experiment. *J. Geophys. Res.* **101**, 3747–3764.

GENT, P. R. & TAYLOR, P. A. 1976 A numerical model of the air flow above water waves. *J. Fluid Mech.* **77**, 105–128.

GENT, P. R. & TAYLOR, P. A. 1977 A note on 'separation' over short wind waves. *Boundary-Layer Meteorol.* **11**, 65–87.

HARA, T. & SULLIVAN, P. P. 2015 Wave boundary layer turbulence over surface waves in a strongly forced condition. *J. Phys. Oceanogr.* **45**, 868–883.

HASEGAWA, Y. & KASAGI, N. 2008 Systematic analysis of high Schmidt number turbulent mass transfer across clean, contaminated and solid interfaces. *Intl J. Heat Fluid Flow* **29**, 765–773.

HOYAS, S. & JIMÉNEZ, J. 2006 Scaling of the velocity fluctuations in turbulent channels up to $Re_\tau = 2003$. *Phys. Fluids* **18**, 011702.

HRISTOV, T. S., MILLER, S. D. & FRIEHE, C. A. 2003 Dynamical coupling of wind and ocean waves through wave-induced air flow. *Nature* **422**, 55–58.

JÄHNE, B. & HAUßECKER, H. 1998 Air–water gas exchange. *Annu. Rev. Fluid Mech.* **30**, 443–468.

JEONG, J. & HUSSAIN, F. 1995 On the identification of a vortex. *J. Fluid Mech.* **285**, 69–94.

https://doi.org/10.1017/jfm.2017.164 Published online by Cambridge University Press

JOHNSON, H. K., HØSTRUP, J., VESTED, H. J. & LARSEN, S. E. 1998 On the dependence of sea surface roughness on wind waves. *J. Phys. Oceanogr.* **28**, 1702–1716.

KADER, B. A. 1981 Temperature and concentration profiles in fully turbulent boundary layers. *Intl J. Heat Mass Transfer* **24**, 1541–1544.

KATSOUVAS, G. D., HELMIS, C. G. & WANG, Q. 2007 Quadrant analysis of the scalar and momentum fluxes in the stable marine atmospheric surface layer. *Boundary-Layer Meteorol.* **124**, 335–360.

KATUL, G. G., SEMPREVIVA, A. M. & CAVA, D. 2008 The temperature–humidity covariance in the marine surface layer: a one-dimensional analytical model. *Boundary-Layer Meteorol.* **126**, 263–278.

KAWAMURA, H., OHSAKA, K., ABE, H. & YAMAMOTO, K. 1998 DNS of turbulent heat transfer in channel flow with low to medium-high Prandtl number fluid. *Intl J. Heat Fluid Flow* **19**, 482–491.

KIHARA, N., HANAZAKI, H., MIZUYA, T. & UEDA, H. 2007 Relationship between airflow at the critical height and momentum transfer to the traveling waves. *Phys. Fluids* **19**, 015102.

KIM, J. & MOIN, P 1986 The structure of the vorticity field in turbulent channel flow. Part 2. Study of ensemble-averaged fields. *J. Fluid Mech.* **162**, 339–363.

KIM, J. & MOIN, P. 1989 Transport of passive scalars in a turbulent channel flow. In *Turbulent Shear Flows 6* (ed. J.-C. André, J. Cousteix, F. Durst, B. E. Launder, F. W. Schmidt & J. H. Whitelaw), pp. 85–96. Springer.

KIM, J., MOIN, P. & MOSER, R. 1987 Turbulence statistics in fully developed channel flow at low Reynolds number. *J. Fluid Mech.* **177**, 133–166.

KITAIGORODSKII, S. A. & DONELAN, M. A. 1984 Wind–wave effects on gas transfer. In *Gas Transfer at Water Surfaces* (ed. W. Brutsaert & G. H. Jirka). Reidel.

LEE, M. & MOSER, R. D. 2015 Direct numerical simulation of turbulent channel flow up to $Re_\tau \approx 5200$. *J. Fluid Mech.* **774**, 416–442.

LI, P. Y., XU, D. & TAYLOR, P. A. 2000 Numerical modeling of turbulent airflow over water waves. *Boundary-Layer Meteorol.* **95**, 397–425.

LIGHTHILL, M. J. 1962 Physical interpretation of the mathematical theory of wave generation by wind. *J. Fluid Mech.* **14**, 385–398.

MEIRINK, J. F. & MAKIN, V. K. 2000 Modelling low-Reynolds-number effects in the turbulent air flow over water waves. *J. Fluid Mech.* **415**, 155–174.

MILES, J. W. 1957 On the generation of surface waves by shear flows. *J. Fluid Mech.* **3**, 185–204.

MOSER, R. D., KIM, J. & MANSOUR, N. N. 1999 Direct numerical simulation of turbulent channel flow up to $Re_\tau = 590$. *Phys. Fluids* **11**, 943–945.

NA, Y., PAPAVASSILIOU, D. V. & HANRATTY, T. J. 1999 Use of direct numerical simulation to study the effect of Prandtl number on temperature fields. *Intl J. Heat Fluid Flow* **20**, 187–195.

PAPAVASSILIOU, D. V. & HANRATTY, T. J. 1997 Interpretation of large-scale structures observed in a turbulent plane Couette flow. *Intl J. Heat Fluid Flow* **18**, 55–69.

PARK, T. S., CHOI, H. S. & SUZUKI, K. 2004 Nonlinear k–ϵ–f_μ model and its application to the flow and heat transfer in a channel having one undulant wall. *Intl J. Heat Mass Transfer* **47**, 2403–2415.

POPE, S. B. 2000 *Turbulent Flows*. Cambridge University Press.

ROBINSON, S. K. 1991 Coherent motions in the turbulent boundary layer. *Annu. Rev. Fluid Mech.* **23**, 601–639.

ROSSI, R. 2010 A numerical study of algebraic flux models for heat and mass transport simulation in complex flows. *Intl J. Heat Mass Transfer* **53**, 4511–4524.

RUTGERSSON, A. & SULLIVAN, P. P. 2005 The effect of idealized water waves onthe turbulence structure and kinetic energy budgets in the overlying airflow. *Dyn. Atmos. Ocean* **38**, 147–171.

SCHWARTZ, L. W. 1974 Computer extension and analytic continuation of Stokes' expansion for gravity waves. *J. Fluid Mech.* **62**, 553–578.

SHAW, D. A. & HANRATTY, T. J. 1977 Turbulent mass transfer to a wall for large Schmidt numbers. *AIChE J.* **23**, 28–37.

https://doi.org/10.1017/jfm.2017.164 Published online by Cambridge University Press

SMITH, S. D. 1988 Coefficients for sea surface wind stress, heat flux and wind profiles as a function of wind speed and temperature. *J. Geophys. Res.* **93**, 15467–15472.

STEWART, R. H. 1970 Laboratory studies of the velocity field over deep-water waves. *J. Fluid Mech.* **42**, 733–754.

STOKES, G. G. 1847 On the theory of oscillatory waves. *Trans. Camb. Phil. Soc.* **8**, 441–455.

SULLIVAN, P. P., EDSON, J. B., HRISTOV, T. S. & MCWILLIAMS, J. C. 2008 Large-eddy simulations and observations of atmospheric marine boundary layers above nonequilibrium surface waves. *J. Atmos. Sci.* **65**, 1225–1245.

SULLIVAN, P. P. & MCWILLIAMS, J. C. 2002 Turbulent flow over water waves in the presence of stratification. *Phys. Fluids* **14**, 1182–1194.

SULLIVAN, P. P. & MCWILLIAMS, J. C. 2010 Dynamics of winds and currents coupled to surface waves. *Annu. Rev. Fluid Mech.* **42**, 19–42.

SULLIVAN, P. P., MCWILLIAMS, J. C. & MOENG, C.-H. 2000 Simulation of turbulent flow over idealized water waves. *J. Fluid Mech.* **404**, 47–85.

TOBA, Y., SMITH, S. D. & EBUCHI, N. 2001 Historical drag expressions. In *Wind Stress over the Ocean*. (ed. I. S. F. Jones & Y. Toba), pp. 35–53. Cambridge University Press.

TSENG, Y.-H. & FERZIGER, J. H. 2003 A ghost-cell immersed boundary method for flow in complex geometry. *J. Comput. Phys.* **192**, 593–623.

VINOKUR, M. 1974 Conservation equations of gas-dynamics in curvilinear coordinate systems. *J. Comput. Phys.* **14**, 105–125.

WALLACE, J. M. 2016 Quadrant analysis in turbulence reserach: history and evolution. *Annu. Rev. Fluid Mech.* **48**, 131–158.

YANG, D., MENEVEAU, C. & SHEN, L. 2013 Dynamic modelling of sea-surface roughness for large-eddy simulation of wind over ocean wavefield. *J. Fluid Mech.* **726**, 62–99.

YANG, D., MENEVEAU, C. & SHEN, L. 2014*a* Effect of downwind swells on offshore wind energy harvesting – a large-eddy simulation study. *J. Renew. Energy* **70**, 11–23.

YANG, D., MENEVEAU, C. & SHEN, L. 2014*b* Large-eddy simulation of offshore wind farm. *Phys. Fluids* **26**, 025101.

YANG, D. & SHEN, L. 2009 Characteristics of coherent vortical structures in turbulent flows over progressive surface waves. *Phys. Fluids* **21**, 125106.

YANG, D. & SHEN, L. 2010 Direct-simulation-based study of turbulent flow over various waving boundaries. *J. Fluid Mech.* **650**, 131–180.

YANG, D. & SHEN, L. 2011*a* Simulation of viscous flows with undulatory boundaries. Part I: basic solver. *J. Comput. Phys.* **230**, 5488–5509.

YANG, D. & SHEN, L. 2011*b* Simulation of viscous flows with undulatory boundaries. Part II: coupling with other solvers for two-fluid computations. *J. Comput. Phys.* **230**, 5510–5531.

YANG, J. & BALARAS, E. 2006 An embedded-boundary formulation for large-eddy simulation of turbulent flows interacting with moving boundaries. *J. Comput. Phys.* **215**, 12–40.

ZANG, Y., STREET, R. L. & KOSEFF, J. R. 1994 A non-staggered grid, fractional step method for time-dependent incompressible Navier–Stokes equations in curvilinear coordinates. *J. Comput. Phys.* **114**, 18–33.

ZEDLER, E. A. & STREET, R. L. 2001 Large-eddy simulation of sediment transport: currents over ripples. *ASCE J. Hydraul. Engng* **127**, 444–452.

https://doi.org/10.1017/jfm.2017.164 Published online by Cambridge University Press